Princeton Plasma Physics Laboratory

PPPL- 4510

PPPL- 4510

Quiet Periods in Edge Turbulence Preceding the L-H Transition in NSTX

S.J. Zweben, R.J. Maqueda, R. Hager, K. Hallatschek, S.M. Kaye,
T. Munsat, F.M. Poli, A.L. Roquemore, Y. Sechrest, D.P. Stotler

April, 2010

Prepared for the U.S. Department of Energy under Contract DE-AC02-09CH11466.

Princeton Plasma Physics Laboratory
Report Disclaimers

Full Legal Disclaimer

Trademark Disclaimer

PPPL Report Availability

Princeton Plasma Physics Laboratory:

http://www.pppl.gov/techreports.cfm

Office of Scientific and Technical Information (OSTI):

http://www.osti.gov/bridge

Related Links:

U.S. Department of Energy

Office of Scientific and Technical Information

Fusion Links

Quiet Periods in Edge Turbulence Preceding the L-H Transition in NSTX

S.J. Zweben[1], R.J. Maqueda[1], R. Hager[2], K. Hallatschek[2], S.M. Kaye[1], T. Munsat[3], F.M. Poli[4], A.L. Roquemore[1], Y. Sechrest[3], D.P. Stotler[1]

[1] Princeton Plasma Physics Laboratory, Princeton, NJ 08540
[2]Max-Planck-Institute for Plasma Physics, Garching, Germany
[3]Univ. Colorado, Boulder CO 80309
[4]University of Warwick, Coventry CV4 7AL, UK

Abstract

This paper describes the first observations in NSTX of 'quiet periods' in the edge turbulence preceding the L-H transition, as diagnosed by the GPI diagnostic near the outer midplane separatrix. During these quiet periods the GPI D_α light emission pattern was transiently similar to that seen during H-mode, i.e. with a relatively small fraction of the GPI light emission located outside the separatrix. These quiet periods had a frequency of ~3 kHz for at least 30 msec before the L-H transition, and were correlated with changes in the direction of the local poloidal velocity. The GPI turbulence images were also analyzed to obtain an estimate for the dimensionless poloidal shearing $S = (dV_p/dr)(L_r/L_p)\tau$. The values of S were strongly modulated by the quiet periods, but not otherwise varying for at least 30 msec preceding the L-H transition. Since neither the quiet periods nor the shear flow increased significantly immediately preceding the L-H transition, neither of these appears to be the trigger for this transition, at least for these cases in NSTX.

I. Introduction

The L-H transitions in tokamaks and similar devices normally occurs very rapidly (<1 msec), but the cause or 'trigger' of these transitions is still not well understood despite more than 25 years of intense experimental and theoretical research [1]. There have been many theoretical models for the L-H transition [2,3], some of which attribute the transition to a the reduction of edge turbulence caused by an increase in the edge radial electric field and poloidal shear flow. Such an increase could be due to fast ion loss, to self-generated mean flows driven by Reynold's stress, or to oscillating zonal flows or geodesic acoustic modes (GAMs).

There is clear experimental evidence for a fast reduction in the level of edge turbulence at the L-H transition, and for an increase in the edge radial electric field and poloidal flows across the transition, but, since these happen nearly simultaneously the causal relationship between them is not well understood [4-7]. Although there have been analytic models and simulations which seemed to explain some aspects of this transition [e.g. 8-11], there is presently no validated computational model available to predict the transition in present or future tokamak devices. This is important since H-mode confinement is required for successful operation of future tokamak reactors, and it is not clear from empirical scalings whether this can be obtained.

The most recent experimental work on L-H transitions has focused on the effects of oscillating zonal flows and GAMs. For example, a 'zero mean field zonal flow" (ZMF-ZF) was observed in DIII-D preceding the L-H transition [12]. In the TJ-II stellarator the turbulence reduction at the transition was coincident with the increase in the low frequency oscillating sheared flow, but *preceded* the increase in the mean shear flow [13]. There is also evidence for coherent oscillating flows associated with GAMs in the edge (but not the scrape-off-layer) [e.g. 14-15], but no direct evidence that the GAMs cause the L-H transition. There is also evidence of a general correlation between zonal flows and the turbulence levels in plasmas [4,5] and fluids [16], but the relationship to the L-H transition is still unclear.

The goal of the present paper is to evaluate the 2-D edge turbulence characteristics and poloidal flow shear preceding the L-H transition in NSTX. The data was acquired using the gas puff imaging diagnostic (GPI) on NSTX. The GPI diagnostic on NSTX previously showed a clear

reduction in turbulence at the L-H transition [17], but with little or no change in correlation lengths or poloidal flow speeds from before to after the L-H transition. However, those measurements were limited to 300 time frames/shot (1.2 msec), and so could only capture a few transitions and were of limited use for studying changes preceding the transition. Additional fast PM tube detectors radial arrays were also used to examine the bicoherence just prior to the transition [18], but those were limited to 13 spatial channels.

The present paper describes new L-H transition measurements made in NSTX using an improved fast camera system which can record 2-D turbulence images at ≤285,000 frames/sec at a resolution of 64x64 pixels for up to 50 msec. This hardware improvement allows the turbulence preceding the L-H transition to be captured for many shots, which was not possible previously. Section II describes the GPI diagnostic, Sec. III describes observations of 'quiet periods' preceding the L-H transition, Sec. IV describes the turbulence shear flows, Sec. V describes a larger database, and Sec. VI contains the Discussion.

II. GPI diagnostic in NSTX

The gas puff imaging (GPI) diagnostic on NSTX (R_o=85 cm, a=65 cm) has been described in detail elsewhere [17-20]. For the present paper the turbulent fluctuations are measured by the excitation of the visible D_α (656 nm) line emission from a deuterium gas puff. Since the turbulence is highly elongated along the magnetic field B, the visible light from the GPI gas puff cloud was viewed along the local B field (to within a few degrees) to resolve the radial vs. poloidal structure of the turbulence. The GPI gas cloud increases the brightness of the D_α by ~x20 above background, and thus localizes the emission for improved spatial resolution.

Figure 1(a) shows a schematic view of the GPI diagnostic geometry in NSTX, including a turbulence filament aligned along B and its intersection with the GPI gas cloud ("blob"). Figure 1(b) shows the location of the GPI field of view, which is centered ~20 cm above the outer midplane near the separatrix, and extends ~ 25 cm radially and ~ 25 cm poloidally. The spatial resolution of the optics is ~ 0.3 cm and the spatial resolution set by the curvature of the field lines within the GPI gas cloud is ≤1 cm. This is small

enough to resolve the edge turbulence structures in NSTX, which have a typical correlation length of ~3-5 cm.

The fast cameras used for this experiment were the Phantom 7.3 and 7.1 from Vision Research. To get the highest possible framing rate for this experiment, two cameras viewed the same GPI image using a beam splitter, and their recording times were interlaced. This allowed a framing rate of up to 285,000 frames/sec (3.5 μs/frame), with an exposure time of 3 μs/frame and at 64x64 pixel resolution. This is only slightly higher than the 250,000 frames/sec rate of the PSI-5 camera used previously [17], but more importantly, these Phantom cameras allow the capture of typically 17,000 frames/shot, whereas the PSI-5 camera allowed only 300 frames/shot. Therefore at the highest framing rate the present cameras recorded ~50 msec/shot, which made it relatively easy to capture L-H transitions.

Typical images from the camera are shown in Fig. 2 for L-mode (left) and H-mode (right), both taken with an exposure time of 3 μsec. The L-mode case shows a complex pattern of D_α typical of edge turbulence, while the H-mode image shows a single poloidal band consistent with a quiescent plasma. These images are oriented with the local minor radial direction approximately horizontal (outward to the right) and the local poloidal direction (within a magnetic flux surface) approximately vertical, with the ion diamagnetic and grad-B drift direction downward. The GPI light intensity is shown in a linear false color scale, the location of the separatrix (according to the PPPL code LRDFIT) is shown by the dashed line, and the location of the shadow of the nearest limiter (RF antenna) is shown by the dotted line to the right. The separatrix location is uncertain to roughly ±1-2 cm (see Sec. VI.C). The GPI gas manifold is located just outside the limiter shadow. The GPI light (D_α emission) is mainly located within ±5 cm of the separatrix in L-mode, and peaks slightly inside the separatrix in H-mode. The box in the center of Fig. 2 shows the radial and poloidal range used for GPI data analysis (± 4 cm around the separatrix), although much of the analysis is done in the middle of this box near the separatrix.

The interpretation of the GPI images has been described previously [17-21]. The D_α light emission is located in the region where the neutrals are excited but not yet ionized, which corresponds roughly to $T_e \approx$ 5-100 eV. Within this temperature range the line emission at a given neutral density is a nonlinear (but monotonically increasing) function of the local electron

density n_e and electron temperature T_e, while the neutral deuterium density is monotonically decreasing toward the plasma center. The radial profiles of D_α light are consistent with DEGAS 2 calculations based on the measured profiles and neutral gas transport from the gas manifold [21].

Although the GPI light emission is a nonlinear function of the local density and temperature, the structure and motion of the GPI light fluctuations, as determined by the space-time cross-correlation functions, is nearly independent of the details of this nonlinearity, as discussed previously [17]. This effect is similar to a TV image in which the structure and motion of an object is independent of the nonlinearity controlled by the contrast setting. Thus the turbulence correlation lengths, times, and speeds can be calculated directly from the GPI data. However, the GPI diagnostic is not able to measure either the absolute or relative density fluctuation level, since the observed D_α emission is a function of both density and temperature, and neither of these is known on the relevant fast timescale.

III. Quiet periods

GPI data was acquired and analyzed for the discharges and plasma conditions listed in Table 1. This data set includes nine shots with an L-H transition captured at the highest available frame rate of (3.5 μsec/frame), four shots with L-H transitions captured at a slower frame rate, two shots in L-mode only, and one shot in H-mode only. Most of the analysis in Secs. 3 and 4 is done for three typical shots in this list (#135042-135044), which had identical external parameters. The larger database is discussed in Sec. V.

Fig. 3 shows the time dependence of D_α light emission from the GPI diagnostic within a ~1.5 cm wide region radially centered at ρ=0.4 cm (with respect to the separatrix), and 15 cm high in the poloidal direction (see box in Fig. 2). The GPI signal from this region dropped rapidly at the H-mode transition at ~0.2454 sec, at about the same time as the standard (but much slower) D_α light emission below. At the right of Fig. 3 are the Thomson scattering profiles just before and just after the H-mode transition in this shot (#135042), showing the formation of a strong 'transport barrier' in the edge density near the separatrix (labeled "sep."). The times of this Thomson scattering data are shown at the bottom left; thus this barrier was formed ≤3

msec after the transition. The radial range of the GPI diagnostic with respect to the outer midplane flux surfaces is also indicated by the arrows at the right in Fig. 3; the GPI view extends radially ~10 cm inside and ~15 cm outside the separatrix. The edge barrier in these cases is formed in the density and not the temperature, and the top of the barrier pedestal in H-mode is just inside the peak of the GPI light emission in Fig. 2.

Fig. 4 shows the time dependence of the GPI signals during a ~10 msec period near the L-H transition (red vertical line) for three shots for the same spatial region as Fig. 3 . In each of these shots there appears to be a series of transient 'quiet' periods of low GPI signal level preceding the transition, several of which are circled in red. These quiet periods have a GPI signal level in this region nearly as low as that ≤2 msec after the transition. Later in the H-mode phase the GPI signals shows stronger intermittent bursts, which will not be discussed in this paper.

Figure 5 shows the sequence of GPI images for a typical ~250 μs period near one of the quiet times circled in red in Fig. 4 (#135044 @ 0.24225-0.244466 sec). Each frame has an exposure time of 3 μsec, the time between frames is 3.5 μsec, and the approximate location of the separatrix is shown by the vertical line in each frame. The quiet period between the frames labeled "Q" in Fig. 5 lasts for ~16 frames, i.e. 60 μs. During this period the GPI images look more similar to those during H-mode than to L-mode (see Fig. 2).

Therefore an empirical way to characterize the quietness of the GPI data is to calculate the fraction of the GPI light emission located radially outside the separatrix, which we will call the "edge quietness parameter" F_{sol}. This parameter is an indirect measure of fast changes in the radial profile shapes of density and temperature near the separatrix, which cause these changes in the profile of D_α. This fraction is shown in Fig. 6 over a longer period of time around the L-H transition for the same three shots as for Fig. 5. The red lines vs. time are this fraction smoothed over 0.7 msec (200 frames), and the dashed line at 0.15 is just shown as a reference. In all cases the F_{sol} drops rapidly at the transition (vertical red lines), corresponding to the change in the emission profiles illustrated in Fig. 2. These 'quiet periods' with F_{sol} <0.15 occur for at least 10 msec before the transition. It appears in these cases as if F_{sol} is slowly decreasing in the ~10 msec before the transition, but this is not a universal feature of the broader database, as discussed in Sec. V.

To further clarify the nature of the quiet periods, Fig. 7(a) plots the radial profiles of the images during the L-mode period in Fig. 4 for #135042, sorted according to their edge quietness parameter F_{sol}. The curve in dark blue labeled "L-mode" includes all the images in the L-mode time period (0.238455-0.245105 sec), and the curve in red labeled "H-mode" includes all images in the H-mode period just after the transition when F_{sol} is lowest (0.245445-0.248340 sec). The curves in light blue, green, and purple include only images in L-mode with signal levels below F_{sol} = 0.15, 0.2, and 0.4 (respectively). Thus the quietest periods in L-mode have radial D_α profiles which look like those seen after the L-H transition. Figure 7(b) shows the radial profile of the relative GPI rms fluctuation level (normalized to its mean) vs. F_{sol} for the same data. The fluctuation level profiles of the quiet periods in L-mode are also similar to those in H-mode, i.e. with a lower relative fluctuation level in the SOL. The relative fluctuation levels inside the separatrix do not significantly change during the quiet periods, although the propagation direction there does change with the quiet periods (see below). The red shaded region indicates the approximate width of the pedestal region the during H-mode period. Similar results are obtained for shots #135043 and 135044.

Figure 8 shows the dynamics of the radial and poloidal profiles of the GPI data for a time ~2 msec before to ~0.5 msec after the L-H transition for shot #135044. Part (a) shows the time dependence of the GPI light vs. radius within a row of pixels at the vertical center of the images, part (b) shows the time dependence of the GPI light vs. poloidal distance in a column of pixels near the separatrix at $\rho \sim 0$, and part (c) shows the time dependence of the GPI light vs. poloidal distance in a column of pixels well inside the separatrix at $\rho \sim -3$ cm where the GPI light peaks during H-mode. The corresponding edge quietness parameter F_{sol} levels are shown by the bands at the right, where white is $F_{sol}=1$ and black is $F_{sol}=0$. The quiet periods are labeled with Q, the H-mode period is labeled as H, the transition is shown as a horizontal dashed line, and the separatrix is shown as a vertical dashed line in (a).

In Figure 8 there are five H-mode-like quiet periods during the 2 msec preceding the transition, not quite evenly spaced in time. Between the quiet periods there are faster bursts or 'blobs' of GPI light extending well into the SOL with a radially outward direction of motion (tilted downward and to the right). In part (b) the quiet periods near the separatrix start from the right side, which is at the top of Fig. 2, and the fast bursts between the quiet

periods largely propagate in the ion diamagnetic direction, i.e. downward to the left. In part (c) the fast bursts during the quiet periods propagate mainly in the electron diamagnetic direction, i.e. downward to the right. Occasional counter-propagating bursts can also be seen in (b) and (c). Thus they dynamics of the turbulence varies with radius and time, as discussed further in Sec. IV.

To examine the time dependence of the quiet periods, Figure 9(a) shows the autocorrelation function of F_{sol} vs. delay time for the same three shots as in Fig. 6, averaged over a 10 msec period preceding the L-H transition in each case. These autocorrelation functions all have a quasi-periodic structure with a period of ~300-400 μs, which is much longer than the typical turbulence autocorrelation time of ~ 8 μsec (see below). This periodicity of the quiet times in the SOL is also visible in the raw data of Figs. 5 and 8. Figure 9(b) shows the power spectra of F_{sol} for the same data, which has relatively broad peaks at a frequency of ~3 kHz, corresponding to the main oscillations in Fig. 9(a). This 3 kHz peak represents a slow coherent modulation of the normal turbulence spectrum, which extends over a broad frequency range of ~1-100 kHz.

Thus Figs. 5-9 show evidence for quasi-periodic H-mode-like "quiet periods" in the D_α light emission near the separatrix for at least 10 msec preceding to the main L-H transition. The following section describes the connection between these quiet periods and other time-dependent statistical analyses of the GPI data, including the local poloidal flow shear.

IV. Turbulence Shear Flows

Figure 10(a) shows the time dependence of the edge quietness parameter F_{sol} during a ~3.5 msec period just before and across the L-H transition, along with several other turbulence properties computed from the same GPI image data for shot #135042. Figure 10(b) shows these same quantities over a longer 17.5 msec period for the same shot. All of these turbulence quantities were evaluated near the separatrix at ρ=0.4 cm. They were averaged over the vertical (i.e. poloidal) range shown in the box in Fig. 2, and also averaged over a time interval of ~40 μsec (11 frames) around each time point. The calculation methods for these turbulence quantities are described in Appendix A. The shaded bands in Fig. 10 approximately mark

the quiet periods near the minima of F_{sol}. The L-H transition occurs just after the last quiet period at ~ 0.2455 sec in this shot.

At the top left of both Fig. 10(a) and (b) is the time dependence of F_{sol} (same as the top panel of Fig. 6), and just below that is the estimated poloidal turbulence velocity V_{pol} within this same region, as calculated from time-dependent cross-correlation functions in the poloidal direction (see Appendix A). Positive V_{pol} corresponds to the electron diamagnetic direction. Below that is the autocorrelation time τ, and at the top right are the poloidal and radial correlation lengths L_{pol} and L_{rad} at the same radius ρ=0.4 cm. All of these turbulence quantities are at least partially modulated with the quiet periods in F_{sol}. For example, the poloidal velocity changes from ~ -2 km/sec between quiet periods to ~ +4 km/sec near the quiet periods, and the poloidal correlation lengths increase from ~4 cm to ~10 cm at the frequency of the quiet periods. Note that the frequency of the quiet periods seems to decrease just before the transition in this case, but this is not generally true (see below). The cross-correlations of various quantities with F_{sol} are described below. These edge turbulence quantities are about the same as seen previously with GPI on NSTX [17].

At the bottom right of Fig. 10(a) and (b) are the "normalized shear", defined here as $S=(dV_p/dr)(L_r/L_p)\tau$, which is a measure of the dimensionless poloidal flow shear determined from the turbulence itself (i.e. not from the plasma ExB flow speed). The quantity S measures the degree to which the average poloidal flow shear tends to distort a turbulent structure within an autocorrelation time at a fixed point. The velocity gradient used in S was evaluated by a linear fit to the poloidally-averaged poloidal velocities over a radial range of $\delta\rho$~1.5 cm centered at ρ=0.4 cm. The velocity gradients found using wider radial ranges of $\delta\rho$~3 cm and $\delta\rho$~5 cm were well correlated with these found using $\delta\rho$~1.5 cm, but systematically up to x2 smaller, as discussed in Appendix A.

Typical values for the pre-transition quantities entering S in the data of Fig. 10 are L_p ~ 4 cm, L_r ~ 3 cm, τ ~ 8 μsec, and dV_p/dr ~ -1 x10^5 sec^{-1}, leading to an typical value of S ~ -1. The range of S for the pre-transition period is mainly between S ~ -2 to 1. Inspection of Fig, 10(a) indicates that S reverses sign near the time of the quiet periods, similarly to the poloidal velocity. From Fig. 10(b) it can be seen that the average behavior of S does not vary significantly over ~15 msec preceding the L-H transition. The

poloidal velocity and S appear to change sign after the L-H transition, but the estimate of S for the H-mode periods just after the transition are not reliable in this data set, since the turbulence levels are very low and the autocorrelation times in H-mode approach the limit of resolution at this framing rate (~3.5 μs).

Figure 11 shows typical time-dependent cross-correlation functions between F_{sol} and other turbulence quantities during a 3.5 msec period just before the L-H transition in #135042 (0.239505-0.243005 sec); namely, (a) F_{sol} vs. V_{pol}, (b) F_{sol} vs. τ, (c) F_{sol} vs. L_{pol}, and (d) F_{sol} vs. S. In this figure the cross-correlations are shown for five radial locations within the box in Fig. 2, including the region at ρ = +0.4 cm used for Fig. 10 (in green). The cross-correlations of F_{sol} and V_{pol} in (a) all show a peak near zero delay, but the exact time of the peak correlation changes systematically with radius. Since a positive time delay in this figure implies V_{pol} lags F_{sol}, this implies, for example, that V_{pol} slightly lags F_{sol} at ρ = -2.8 cm, and V_{pol} slightly leads F_{sol} at ρ = -+3.6 cm, and. Cross-correlations of F_{sol} and S are strongest near the separatrix, for example, at ρ = +0.4 cm, where S lags F_{sol} by 14 μsec. Thus these patterns of cross-correlation are rather complicated, and there is no single causal (i.e. temporal) relationship between V_{pol} or S and F_{sol}. The detailed spatial structure and frequency spectrum of these flows and correlations will be discussed separately using a velocimetry code with higher space and time resolution [22].

Figure 12 shows the time evolution of several of the quantities of Fig. 11 before the L-H transition for the same three shots as in Fig. 9. Each point in Fig. 12 averages over 3.5 msec (1000 frames), which includes ~10 cycles of the ~3 kHz oscillation. Figure 12(a) shows the magnitude of the first negative peak of the autocorrelation function of F_{sol}, which is a rough measure of the size of the quasi-periodic feature at ~3 kHz, and below that is the corresponding frequency of this feature. Neither of these quantities change significantly over ~30 msec preceding the L-H transition. In Fig. 12(b) is the magnitude of the peak of the cross-correlation functions between F_{sol} and V_{pol} (nearest zero delay time), and below that is the delay time to this peak. Neither of these quantities change significantly over ~30 msec preceding the L-H transition either. Finally, in Fig. 12(c) is the magnitude of the peak of the cross-correlation functions between F_{sol} and S (nearest zero delay time), and below that the delay time to this peak. Again, neither of these quantities change significantly over ~30 msec preceding the L-H

transition. Thus there is no consistent change in these correlations over a ~30 msec timescale preceding the L-H transition. Since the transition happens so rapidly (≤ 1 msec), this strongly suggests that the quiet periods do not cause or trigger the transition.

Finally, Fig. 13 shows scatter plots of the correlation between the edge quietness parameter F_{sol} and V_{pol} (left) and F_{sol} and S (right) for the same ρ=0.4 cm case used for Fig. 11. Here both plots show all 1000 time points within a 3.5 msec period ending ~2 msec before the transition, with a small correction to align the time at the peak of their cross-correlations of Fig. 11. There is clearly only a partial correlation between V_{pol} and F_{sol} in this (and all other) data, but with trend for low values of F_{sol} to occur at positive V_{pol}, as can also be seen in Fig. 10(a). There is a rather wide scatter of F_{sol} vs. S (right), independent of the radial averaging width $\delta\rho$ used for dV_p/dr (i.e. red vs. blue). Thus there is only a partial correlation between S and F_{sol} in this data.

V. Larger database

Table 1 lists the 16 shots in this database, i.e. nine shots with L-H transition captured at the highest available frame rate of (3.5 μsec/frame), four shots with L-H transitions captured at a slower frame rate, two shots in L-mode only, and one shot in H-mode only. This data was analyzed in the same way as #135042-135044 for Figs. 10-12 to check whether the trends described in Sec. 4 were typical.

Figure 14 shows the analysis of the size and frequency of the ~3 kHz quiet feature with respect to the L-H transition time for all of these shots, including the data previously shown in Fig. 12(a). The two L-mode shots are arbitrarily set at -150 msec and the one H-mode shot is set at +50 msec to put them on the same plot. There appears to be no systematic change in the size or frequency of the ~3 kHz feature during the ~30 msec preceding the L-H transition, consistent with Fig. 12. However, there is a significant scatter in the size and frequency over this time period, which may be due to a modulation in the amplitude of the quiet feature, analogous to that seen for the GAM [14]. Also, a qualitatively similar ~3 kHz feature appears in the few L-mode and H-mode shots examined, implying that the quiet periods do not only occur before L-H transitions. Note that the relatively few data

points in Fig. 14 outside ~0-50 msec before the transition is due to absence of data at these times, and not the absence of a 3 kHz feature in the data.

Figure 15 shows the time dependences of F_{sol} and S before the L-H transition for two other high speed shots besides #135042 (already shown in Fig. 10(b)). Although there is a strong modulation of S with F_{sol} at ~3 kHz, as in Fig. 10, there appears to be no systematic change in S within ~15 msec of the transition for these cases, or for any of the 9 shots with the fastest framing rate, consistent with Fig. 10. Note that the two shots in Fig. 15 do not show any systematic decrease in the edge quietness parameter F_{sol} during the few msec before the transition, as seems to be the case for the three shots in Fig. 6.

Figure 16 shows S vs. time for three different radial locations for the time period up to ~1.5 msec before the transition, with shot #135042 at the left, and a superposition of all 9 shots with the fastest framing rate at the right. Again, there appears to be no systematic change in S just before the transition which could be considered as trigger to the L-H transition.

VI. Discussion

A. Summary of results

This paper described the first NSTX observations of 'quiet periods' in the edge turbulence preceding the L-H transition, as diagnosed by the GPI diagnostic near the outer midplane separatrix. During these quiet periods the GPI D_α light emission pattern was transiently similar to that seen during H-mode, i.e. with a small "edge quietness parameter" F_{sol}, defined as the fraction of the GPI light emission located outside the separatrix. These quiet periods had a frequency of ~3 kHz and were observed for at least 30 msec before the L-H transitions. There was some evidence that similar quasi-periodic oscillations occurred during L-mode shots well before the transition, even without any L-H transition, and also well after the L-H transition. Thus these quiet periods appear to occur independent of the L-H transition, and so do not appear to be a trigger or direct cause of the L-H transition in NSTX.

The paper also analyzed the turbulence in the GPI images to obtain an estimate for the dimensionless poloidal shearing $S = (dV_p/dr)(L_r/L_p)\tau$, which measures the extent to which the average poloidal flow shear distorted the turbulence structure within a local turbulence autocorrelation time. The strongest time variation in S was correlated with the presence of the quiet periods, when the poloidal velocity reversed sign and moved dominantly in the electron diamagnetic direction, at least near the separatrix. Apart from this ~3 kHz modulation, there was no significant time variation of S up to 30 msec before the L-H transition within ±3 cm of the separatrix. Thus the flow shear measured in this way does not appear to be a trigger or direct cause of the L-H transition in NSTX.

The cross-correlation coefficient and phase between F_{sol} and V_{pol} changed systematically with radius over the range of radii ρ = -2.8 to 3.6 cm, as shown in Fig. 11(a). This indicates a strong variation across the separatrix of the phase of the poloidal flow associated with the quiet periods. There were also lower cross-correlations between F_{sol} and the other turbulence quantities such as L_{pol} and τ, as shown in Figs. 11(b) and 11(c). Thus the quiet periods were associated with a complicated set of changes in the turbulence structure and motions, which will be examined further elsewhere using a higher resolution velocimetry code[22].

There does not appear to be any systematic precursor or trigger for the L-H transition as seen in this data or analysis. The fast ($\leq$ 1 msec) changes seen at the transition occur at approximately the same time in the SOL and inside the separatrix, as illustrated in Fig. 8, so it is not yet clear where the transition begins in minor radius. There are often (but not always) slower decreases in F_{sol} before the transition ($\leq$10 msec), as shown in Fig. 6, which may indicate gradual changes in the edge profiles leading up to the transition. Possible future ways to clarify the cause of the transition are discussed in Sec. VI.E.

B. Relation to previous experimental results

Previous GPI measurements of turbulence on NSTX [17] used high speed cameras with only 300 frames at 250,000 frames/sec (1.2 msec), so did not identify the slowly oscillating quiet periods described here. However, the poloidal array of PM tubes did detect some transient reversals

in V_{pol} preceding the L-H transition (Fig. 6 of Ref. 17), which are similar to those shown in more detail in Fig. 10 here.

The closest related measurements on tokamaks were done using a 2-D beam emission spectroscopy (BES) diagnostic at the edge of DIII-D [12]. There (as here) the edge turbulence level decreased sharply at the L-H transition, and low frequency oscillations of the poloidal turbulence velocity, called 'zero mean frequency zonal flows', were observed to peak near ~2 kHz in L-mode (Fig. 10 of Ref. 12). Systematic variations were observed in the turbulence, shear flow, and L-H transition with the neutral beam torque, but there were no measurements of 'quiet periods' or local turbulence shear flow in that paper.

There have also been several previous measurements on both tokamaks and other devices which showed a correlation between low frequency zonal flows and the magnitude of higher frequency turbulence, as reviewed in [5,6]. This type of correlation is at least qualitatively similar to the relationship observed here between poloidal flows and quiet periods. However, here there was only a partial correlation between the quiet periods and the local poloidal flow or shear, as illustrated in Figs. 11 and 13, and the phase shifts between these quantities varied with radius. Thus the causal connection between these observed flows and quiet periods is unclear at present.

Previous observations of highly coherent GAMs have been made in many devices and with several diagnostics [e.g. 13-15]. The frequency spectra observed here (Fig. 9) are broader than those previously seen for GAMs, and GAMs have not previously been observed in the SOL, as are the quiet periods here. Thus it is not clear whether these quiet periods are GAMs (see also Sec. 6.D).

The literature on edge turbulence in tokamaks includes analyses of 'quiet-time statistics' between successive bursts of turbulent flux in JET and other devices [23]. However, that analysis found a continuous distribution of quiet times and not a quasi-periodic oscillation in quiet times, as found here (e.g. Fig. 9). Also, that analysis was focused on comparisons with SOC or rescale adjusted range (R/S) models, and not with poloidal flows or local shear, as described here.

Many other previous experimental results related to the L-H transition are reviewed in [4-7]. So far as we know, there has been no previous measurement of the dimensionless turbulence flow shear across the L-H transition based on the local turbulence quantities (radial and poloidal correlation lengths, times, and poloidal flows), as done here using the GPI data. There have been several related measurements of the turbulence levels and turbulent transport associated with flow shear and zonal flows generated by electrode biasing [24], but the relationship between electrode biasing and the spontaneous L-H transitions is not quite clear.

C. Uncertainties and Limitations

The main uncertainty in the present measurements concerns the absence of a direct interpretation of the GPI light emission in terms of the local plasma parameters. Although the measured D_α light is a well known function of the atomic physics $f(n_e,T_e)$ [21], there is no way at present to determine whether GPI profile changes during quiet periods are due to density or temperature changes, or both. Thus the evaluation of local plasma-dependent quantities such as the collisionality or β can not be done using the GPI data. However, turbulence properties such as the correlation lengths, times, velocities, and hence the normalized shear, are independent of the nonlinearities in the $f(n_e,T_e)$ and can be evaluated directly from the GPI data [19].

The location of the separatrix, which has been evaluated here using the NSTX-standard model LDRFIT (i.e. magnetic measurements supplemented by Thomson scattering profiles), is uncertain by roughly ±1-2 cm. However, even though the numerical value of the "edge quietness parameter" F_{sol} used here (e.g. in Fig. 6) depends on the separatrix location, the relative time dependence and spectrum of F_{sol} does not, at least within this range of uncertainty; therefore the results derived from F_{sol} are to a good approximation independent of this separatrix uncertainty. The exact location of the separatrix may eventually be important for interpreting the turbulence changes during quiet periods, which at present seem to be localized in the SOL and not inside the separatrix (see Fig. 7).

The analysis in this paper uses measurable turbulence quantities to evaluate the local poloidal shear flow, i.e. $S = (dV_p/dr)(L_r/L_p)\tau$. Thus the radial electric fields, which play an important role in theory, are not directly

measured here. Also, the autocorrelation time at a fixed point used here is only an approximate measure of the structure lifetime. Typical statistical uncertainties in the estimation of GPI correlation lengths and times and poloidal velocity can be seen in Fig. 10(a) in between the quiet periods, and are roughly ±10-20% for the chosen averaging interval of ~40 μsec. The estimation of the gradient in poloidal velocity requires an additional averaging over some radial range, which was chosen to be the smallest plausible value of ~1.5 cm (4 pixels). The variation in S was reduced by about a factor of 2 when this radial averaging range was increased to ~5 cm, as shown in Fig. 13. Thus the estimate of S is uncertain by at least a factor of two due to the uncertainties in L_{pol}, L_{rad}, τ and dV_{pol}/dr. This uncertainty most likely accounts for the wide scatter in the F_{sol} vs. S plots in Fig. 13, and the less-than-perfect correlations of Fig. 11. However, the plots of Fig. 11 clearly show statistically significant time-averaged cross-correlations between the various turbulence quantities, as described in Sec. IV.

An important limitation of this study comes from the relatively small database (Table 1), which did not allow evaluation of the parameter dependences (e.g. on n_e, B, q, P_{NBI}, etc.). Another limitation was that the GPI diagnostic on NSTX covers only a small range of poloidal angles just above the outer midplane, and could not see far inside the separatrix. There is very limited information available so far from other NSTX diagnostics on the quiet periods or edge shear flow. The standard D_α signals (as in Fig. 3) and the edge poloidal rotation diagnostic do not have a fast enough response to observe either the edge turbulence or the quiet periods, and no correlation of the quiet periods has yet been observed with magnetic fluctuations at the wall, with edge soft x-ray emission, or with the separatrix location as determined by EFIT.

D. Relationships to theory and simulation

The principal theoretical question about these results concerns the physics of the ~3 kHz quiet periods seen in the GPI data preceding the L-H transition. Given recent large body of recent experimental and theoretical work in the area of zonal flows [5,6], it is plausible that this is an example of a zonal flow or a GAM. As already mentioned in Sec. VI.B, the spectrum of the quiet periods is not as sharp as typical for GAMs, and GAMs have not

previous been observed in the SOL, as they are here for the quiet periods. However, a calculation of the GAM frequency for NSTX was done by solving the eigenvalue problem given by the two-fluid equations as used in the NLET code [26] for zero radial wavenumber, with the result:

$$f(\mathrm{Hz}) = (1/(\pi R)\, c_s\, G \qquad [1]$$

where R is the major radius at the outboard midplane of the considered flux surface, c_s is the thermal speed $[\gamma(T_i+T_e)/m_i]^{1/2}$, γ is the adiabatic exponent of the system (ranging between 1 and 5/3 for isothermal and adiabatic systems, respectively), and G is the geometry dependent factor determining the GAM frequency.

The GAM originates from the coupling between sound waves and poloidal rotation induced by the toroidal curvature. While in a large aspect ratio tokamak with circular flux surfaces, the poloidal rotation couples in principle only to the sinusoidal (n=0,m=1) pressure perturbation resulting in one high frequency mode – the GAM – in more complicated setups as in NSTX, the poloidal rotation can couple to several sound modes resulting in several modes which to some extent show GAM behavior. The 'GAM-ness' of those modes can be classified by the ratio of the mean energy of the poloidal flow to the mean parallel kinetic energy of the mode, E_{perp}/E_{par}, which is evaluated using the velocity fields from the numerical solution of the GAM eigenvalue problem mentioned above. Modes with $E_{perp} >\sim E_{par}$ can be called GAMs whereas modes with $E_{perp} << E_{par}$ are practically sound waves.

The frequency spectrum for NSTX near the separatrix calculated this way contains three modes that can be considered GAMs, namely G~0.49, 0.31 and 0.65 with E_{perp}/E_{par}~1.48, 1.03 and 0.67, respectively. Due to the similar ratios E_{perp}/E_{par} in principle all three modes can be present in a turbulent system. Eventually, the properties of the turbulence decide whether one mode is excited preferentially. The T_e measured by Thomson scattering at the separatrix in L-mode was ~ 50 eV (Fig. 3). Thus, assuming $T_i \sim T_e$ and R=1.5 m, the expected GAM frequency is in the range ~4.6-12.3 kHz for the three GAM candidates (using G=0.31 with γ=1 and G=0.65 with γ=5/3). Numerical 3D-turbulence studies using NSTX geometry performed with NLET show that the 'low frequency' GAM candidate is excited by the turbulent modes. The observed GAM frequency of f~6.3 kHz at T_e=50 eV is slightly higher than the upper limit of the mode with G~0.31 predicted from

the linear calculation above. Hence, the GAM frequency predicted by NLET is of the same order as the frequency of the quiet periods, which is quite good agreement, considering the large temperature variation of T_e~10 to 100 eV within ± 2cm around the separatrix.

E. Conclusions and Future work

There were two main conclusions from this paper: (1) transient quiet periods were found in the edge turbulence in NSTX which correlated with local reversals in direction of the poloidal flow and flow shear, and (2) neither the quiet periods nor the poloidal shear flow were the trigger for the L-H transitions in NSTX, since neither changed significant over ~30 msec preceding the transition. This latter (negative) result supports the conclusion of a recent review that "the role of turbulence in triggering the L-H transition must be considered open" [5].

The most important future work involves the search for such a trigger. One possibility is that the L-H transition does just not have any clear precursor in the edge turbulence, but is caused when slow or slight changes crosses some threshold to produce a sudden 'phase transition'. Another possibility is that the trigger is non-local, i.e. the changes seen in the GPI diagnostic were caused by events outside the field of view, e.g. far inside the separatrix or in the divertor region. A third possibility is that the trigger event involves complex or subtle changes in the local turbulence which have not been identified yet.

Future work will examine in detail the frequency spectrum and radial structure of the turbulence flows in these data using a sophisticated hybrid optical flow/pattern (HOP-V) matching code [22], which has a higher space-time resolution than the cross-correlation analysis used in the present paper. An initial comparison of the poloidal velocities inferred from that code with the present cross-correlation velocity analysis show good agreement, as described in the Appendix. The HOP-V codes also shows that the phase of V_{pol} changes from inside to outside the separatrix, similar to the cross-correlation results shown in Fig. 11(a) here.

Bicoherence analysis of the GPI turbulence in NSTX has been done previously [18]. More recent analysis [29] shows that the quiet periods are well correlated with minima in the level of bicoherence for all frequencies,

and during quiet periods of longer duration, such as those circled in Fig. 4, a gradual increase in the bicoherence is measured, associated with interactions between low frequency and intermediate to large frequency fluctuations. Further analysis, including the computation of bicoherence in wavenumber space, will assess this interplay between large and intermediate scales.

Finally, future work should also address the scaling of frequency and size the quiet periods with edge temperature, q(a), collisionality, etc. The poloidal rotation of the turbulence seen with GPI should also be compared with spectroscopic rotation measurements and with neoclassical predictions. Measurements of edge turbulence at another poloidal angle could confirm the zonal nature of the quiet periods and flows. It would also be instructive to examine the possible relationship of these quiet periods with the much slower 'dithering' process often seen in L-H transitions [1].

Acknowledgments: We thank R. Bell, C.S. Chang, E. Fredrickson, T.S. Hahm, C. Hidalgo, S. Kubota, B. LeBlanc, K.C. Lee, R. Maingi, J. Menard, D.E. Newman, D.A. Russell, S.A. Sabbagh, V. Soukhanovskii, K. Tritz and the NSTX Team for their contributions to this paper. This work was supported by US DOE Contracts #DE-AC02-09CH11466 and DE-FG02-08ER54995.

References:

[1] F. Wagner, Plasma Phys. Cont. Fusion 49, B1 (2007)

[2] J. W. Connor and H.R. Wilson, Plasma Phys. Cont. Fusion 42, R1 (2000)

[3] T.S. Hahm, Plasma Phys. Cont. Fusion 44, A87 (2002)

[4] C. Hidalgo, M.A. Pedrosa, B. Goncalves, New J. Physics 4, 51.1 (2002)

[5] G.R. Tynan, A. Fujisawa, and G. McKee, Nucl. Fusion 51, 113001 (2009)

[6] A. Fujisawa, Nucl. Fusion 49, 113001 (2009)

[7] S.J. Zweben, J.A. Boedo, O. Grulke, C. Hidalgo, B. LaBombard, R.J. Maqueda, P. Scarin, J. Terry, Plasma Phys. Cont. Fusion 49, S1 (2007)

[8] B. Rogers, J.F. Drake, A. Zeiler, Phys. Rev. Lett. 81, 4396 (1998)

[9] P.N. Guzdar, R.G. Kleva, R.J. Groebner, and P. Gohil, Phys. Rev. Lett. 89, 265004 (2002)

[10] X. Xu, R.H. Cohen, W.M. Nevins, G.D. Porter, M.E. Rensink, T.D. Rognlien, J.R. Myra, D.A. D'Ippolito, R.A. Moyer, P.B. Synder, T.N. Carlstrom, Nucl. Fusion 42, 21 (2002)

[11] M.A. Malkov and P.H. Diamond, Phys. Plasmas 15, 122301 (2008)

[12] G.R. McKee, F. Gohil, D.J. Schlossberg, J.A. Boedo, K.H. Burrell et al Nucl. Fusion 49, 115016 (2009); D. J. Schlossberg, G. R. McKee, R. J. Fonck, K. H. Burrell, P. Gohil, R. J. Groebner, M. W. Shafer, W. M. Solomon, and G. Wang, Phys. Plasmas 16, 080701 (2009); D.R. Gupta, R.J. Fonck, G.R. McKee, D.J. Schlossberg, and M.W. Shafer, Phys. Rev. Lett. 97, 125002 (2006)

[13] T. Estrada , T. Happel, L. Eliseev D. Lopez-Bruna D , E. Ascasibar, E. Blanco, L. Cupido, J.M. Fontdecaba, C. Hidalgo, R. Jimenez-Gomez, L. Krupnik, M. Liniers, M.E. Manso, K.J. McCarthy, F. Medina, A. Melnikov,

B. van Milligen, M.A. Ochando, I. Pastor, M.A. Pedrosa, F.L. Tabares, D. Tafalla, Plasmas Phys. Cont. Fusion 51, 124015 (2009)
[14] G.D. Conway and the ASDEX Upgrade Team, Plasma Phys. Cont. Fusion 50, 085005 (2008)

[15] A.V. Melnikov, V.A. Vershkov, L.G. Eliseev, S.A. Grashin, A.V. Gudozhnik, L.I. Krupnik, S.E. Lysenko, V.A. Mavrin, S.V. Perfilov, S.A. Shelukhin, S.V. Soldatov, M.C. Ufimtsev, A.O. Urazbaev, G. Van Oost, and L.G. Zimeleva, Plasma Phys. Cont. Fusion 48, S87 (2006)

[16] M.G. Shats, H. Xia, H. Punzmann, G. Falkovich, Phys. Rev. Lett. 99, 164502 (2007)

[17] S.J. Zweben, R.J. Maqueda, J.L. Terry, J.R. Myra, D. D'Ippolito, D.A. Russell, J.A. Krommes, B. LeBlanc, T. Stoltfus-Dueck, D.P. Stotler, K.M. Williams, C.E. Bush, R. Maingi, O. Grulke, S.A. Sabbagh, A.E. White, Phys. Plasmas 13, 056114 (2006)

[18] A.E. White, S.J. Zweben, M.J. Burin, T.A. Carter, T.S. Hahm, J.A. Krommes, R.J. Maqueda, Phys. Plasmas 13, 072301 (2006)

[19] S.J. Zweben, R.J. Maqueda, D.P. Stotler, A. Keesee, J. Boedo, C.E. Bush , S.M. Kaye, B. LeBlanc, J.L. Lowrance, V.J. Mastrocola, R. Maingi, N. Nishino, G. Renda, D.W. Swain, J.B. Wilgen and the NSTX Team, Nucl. Fusion 44, 134 (2004)

[20] R.J. Maqueda, G.A. Wurden, D.P. Stotler, S.J. Zweben, B. LaBombard, J.L. Terry, J.L. Lowrance, V.J. Mastrocola, G.F. Renda, D.A. D'Ippolito and J.R. Myra, Rev, Sci. Inst. 74, 2020 (2003); R.J. Maqueda and D.P. Stotler, submitted to ??

[21] D. P. Stotler, B. LaBombard, J. L. Terry, and S. J. Zweben, J. Nucl. Mater. 313-316, 1066 (March 2003)

[22] T. Munsat and S.J. Zweben, Rev. Sci. Inst. 77, 103501 (2006); also Y. Sechrest and T. Munsat, private communication (2010)

[23] R. Sanchez, B. Ph. van Milligen, D.E. Newman, and B.E. Carreras, Phys. Rev. Lett. 90 (2003) 185005 ; V.E. Lynch, B.A. Carreras, R. Sanchez, B. LaBombard, B. Ph. van Mulligan, and D.E. Newman, Phys. Plasmas 12,

052304 (2005)

[24] Y. Yu, S. Jachmich, R.R. Weynants, M. Van Schoor, M. Vergote, A. Kramer-Flecken, O. Schmitz, B. Unterberg, C. Hidalgo, and the TEXTOR Team, Phys. Plasmas 16, 110704 (2009); J.A. Boedo, D.S. Gray, P.W. Terry, S. Jachmich, G.R. Tynan, R.W. Conn, and the TEXTOR-94 Team, Nucl. Fusion 42, 117 (2002); T. Carter and J.E. Maggs, Phys. Plasmas 16, 012304 (2009)

[26] K. Hallatschek and A. Zeiler, Phys. Plasmas 7, 2554 (2000)

[27] D.A. Russell, J.R. Myra, D.A. D'Ippolito, Phys. Plasmas 16, 122304 (2009)

[28] Z. Lin, T.S. Hahm, W.W. Lee, W.M. Tang, P.H. Diamond, Phys. Rev. Lett 83, 3645 (1999)

[29] F. Poli, private communication (2010)

Table 1: L-H Transition Database

Shot	Ip (MA)	B (kG)	L-H (s)	GPI data (s)	NBI (MW)	Frame (μsec)
132682	0.8	4.4	0.2544	0.170-0.252	1.9-3.0	8.25
132712	0.8	4.5	0.3375	0.200-0.282	0.9-2.4	8.25
132716	0.8	4.5	-	0.200-0.250	0	8.25
132719	0.8	4.3	-	0.200-0.250	1.7-2.3	8.25
132959	0.92	4.4	0.2525	0.220-0.260	1.2	6.75
132967	0.92	4.4	0.2555	0.220-0.260	2.8	6.75
135020	0.8	4.5	0.1750	0.205-0.260	0.8-2.7	7.0
135021	0.9	4.5	0.2391	0.205-0.260	0.8-2.7	3.5
135022	0.92	4.5	0.2507	0.215-0.260	0.8-2.6	3.5
135023	0.92	4.5	0.2518	0.215-0.260	0.8-4.5	3.5
135041	0.92	4.5	0.2495	0.215-0.275	0.7-2.6	3.5
135042	0.92	4.5	0.2455	0.215-0.275	0.7-2.6	3.5
135043	0.92	4.5	0.2500	0.215-0.275	0.7-2.6	3.5
135044	0.92	4.5	0.2451	0.215-0.275	0.7-2.6	3.5
135045	0.92	4.5	0.2435	0.215-0.275	0.7-2.6	3.5
135046	0.92	4.5	0.2539	0.225-0.275	0.7-2.6	3.5

Appendix A – calculation of turbulence quantities

The turbulence quantities for the analyses in this paper were calculated directly from the GPI light intensity images vs. time (e.g. Fig. 5). The autocorrelation times τ were calculated for each pixel as the time for the autocorrelation function to first go down to 0.5; this τ measures the short turbulence autocorrelation time of ~10 μsec, and does not measure the much longer ~3 kHz oscillation. These results were then the averaged over the ~15 cm high poloidal range of the box shown in Fig. 2, and over ~40 μsec in time (11 frames) to get the τ in Fig. 10. The correlation lengths were calculated as $L = 1.66\ (\delta x) / \mathrm{sqrt}(-\ln C_{12})$, where δx is the radial or poloidal separation between two nearby points and C_{12} is the zero-time cross-correlation coefficient between them (this assumes a Gaussian correlation function). The distances used were δx~1.6 cm in the poloidal direction (4 pixels) and δx~0.8 cm in the radial direction (2 pixels), i.e. both were well within a correlation length. These local correlation lengths were then averaged over the ~15 cm high poloidal range of the box shown in Fig. 2, and over ~40 μsec in time (11 frames) to get the L_{rad} and L_{pol} of Fig. 10.

The poloidal velocity V_{pol} was calculated for each pixel for each frame by first calculating the one-frame-delayed cross-correlation coefficient between that pixel and nearby pixels (±5 pixels each direction), averaging over ±11 frames in time (±38.5 μsec). The poloidal speed for that pixel and frame is then calculated as the poloidal displacement of the peak correlation location divided by the time between frames (typically 1-3 pixels/frame or ~1-3 km/sec). These local poloidal velocities are then averaged over the ~15 cm high poloidal range of the box shown in Fig. 2 to get the V_{pol} shown in Fig. 10, which is for a single radial location. The velocity gradient at that radial location is found by making a linear fit to the V_{pol} values in adjacent radial locations over a radial width of $\delta\rho$, where $\delta\rho$~1.5 cm (±2 pixels) for Figs. 10-12. The results for different radial widths of $\delta\rho$~3 and $\delta\rho$~5 cm are highly correlated with the results for $\delta\rho$~1.5cm (i.e. R=0.9-0.95), but the relative magnitudes of these slopes decreases from 1 to 0.67 to 0.45 over this range, most likely due to averaging over fine scale structure for higher $\delta\rho$. A comparison of results for $\delta\rho$~1.5 cm and $\delta\rho$~5 cm is shown in Fig. 13.

The V_{pol} determined in this way from cross-correlations functions was compared with the V_{pol} determined from the hybrid optical flow-pattern matching code HOP-V [22]. There was a good cross-correlation coefficient of 0.77 between these two velocity time series for a typical shot, when averaged over the same time interval and poloidal pixel range (±40 μsec and 15 cm). The average velocity using the cross-correlation method was ~0.87 times that using HOP-V [22].

Figure Captions:

1) Geometry of the GPI diagnostic in NSTX. In (a) is a sketch of the vessel outer wall (as seen from the plasma) showing the re-entrant GPI viewport, the manifold from which the gas puff emerges, and the approximate angle of the local magnetic field. The 3-D structure of the turbulence is shown as a 'filament', and the 2-D projection of a filaments with the GPI radial vs. poloidal plane is shown as a 'blob'. In (b) is an LRDFIT equilibrium at the L-H transition time for #135042, along with the GPI area projected into the (R, z) plane (green), the location of the GPI manifold (purple), and the projection of the RF antenna/limiter (blue)

2. Typical GPI images of the D_α light emission in this experiment. At the left is an L-mode image and at the right is an H-mode image later in the same shot, both images taken with 3.5 μs exposure times and the same (false) color intensity scale. Also shown is the best estimate for the separatrix location (dashed line, as determined from the LRDFIT code of NSTX), and the shadow of the RF antenna/limiter location (dotted line). These images cover an region ~25 cm in the radial (horizontal) direction and ~25 cm in the poloidal (vertical) directions, and have a pixel size of ~0.4 cm. The range of GPI turbulence analysis is shown by the rectangle in the middle.

3. Time dependence of D_α light emission from the GPI diagnostic within a 1.5 cm wide region just outside the separatrix at ρ=0.4 cm. This GPI signal drops rapidly at the H-mode transition at ~0.2454 sec, at about the same time as the standard D_α light emission signal drops (the latter has a slower response time). At the right are Thomson scattering profiles just before and just after the H-mode transition showing the formation of an edge density transport barrier after the transition. The times of these Thomson scattering data are shown at the bottom left. The radial range of the GPI diagnostic with respect to the outer midplane flux surfaces is also shown at the right, along with the separatrix location (labeled "sep.").

4. Time dependence of the GPI signal during a ~10 msec time period around the L-H transition for the same spatial region as Fig. 4, i.e. just outside the separatrix. Three successive shots are shown which were taken under identical machine conditions. In each of these shots there are several transient 'quiet' periods of low GPI signal level preceding the transition, and

there is an especially quiescent GPI signal level within the time ≤ 2 msec after the L-H transition.

5. Sequence of GPI images for a ~250 μs (70 frame) period showing a typical quiet time (#135044 @ 0.24225-0.244466 sec). Each frame has an exposure time of 3.5 μs, and the approximate location of the separatrix is shown by the vertical line in each frame. This quiet period (labeled "Q") lasts for ~16 frames, i.e. 60 μs. During this time the GPI images look like those seen in H-mode, rather than those usually seen in L-mode (see Fig. 1).

6. Fraction of the GPI light emission located outside separatrix (i.e. edge quietness parameter F_{sol}) vs. time for the same three shots as for Fig. 5. The red lines are this fraction smoothed over 0.7 msec (200 frames), and the dashed line at 0.15 is just shown for reference. In all cases F_{sol} drops rapidly below 0.15 at the L-H transition (red vertical line), but occasionally goes below 0.15 before the L-H transition (quiet periods). Well after the main transition, F_{sol} shows intermittent bursts above $F_{sol} = 0.15$ for the remainder of the H-mode period.

7. Radial profiles and relative fluctuation levels of the GPI data for #135042 for a ~10 msec period preceding the L-H transition, sorted according F_{sol} (fraction of GPI light located outside the separatrix). Part (a) shows that the radial profiles in L-mode during the quiet periods with $F_{sol} < 0.2$ (i.e. light blue and green) look similar to the radial profiles just after the L-H transition (red), whereas the average profile in L-mode is significantly broader (dark blue). Part (b) shows that the relative GPI fluctuation levels for $F_{sol} < 0.2$ are also similar to H-mode fluctuation levels, i.e. smaller than L-mode in the SOL (but not inside the separatrix). The red shaded region indicates the approximate width of the pedestal region the during H-mode period.

8. Fast time dependence of the radial and poloidal profiles of the GPI data from ~2 msec before to ~0.5 msec after the L-H transition for shot #135044. Part (a) shows the time dependence of the GPI light vs. radius across a row of pixels at the vertical center of the images, part (b) shows same time dependence of the GPI light vs. poloidal distance down a column of pixels near the separatrix at ρ ~0, and part (c) shows same time dependence of the GPI light vs. poloidal distance down a column of pixels well inside the separatrix at ρ ~ -3 cm. The corresponding F_{sol} levels are shown in the bars at the right, where white is $F_{sol}=1$ and black is $F_{sol}=0$. The quiet periods are

labeled with a Q, the H-mode period is labeled as H, the L-H transition is the horizontal dashed line, and the separatrix is the vertical dashed line.

9. In (a) are the autocorrelation functions of F_{sol} vs. delay time for the three shots of Fig. 6, averaged over a time 10 msec preceding the L-H transition, and in (b) are the frequency (power) spectra of F_{sol} for the same data. The autocorrelation functions all have a quasi-periodic structure with a period corresponding to a frequency of ~3 kHz. This periodicity of the quiet times in the SOL is also visible in the raw data of Fig. 5 and 8.

10. Part (a) shows the time dependence F_{sol} during a ~3.5 msec period across the L-H transition for shot #135042, along with several other turbulence properties computed from the same GPI image data. The approximate time of the quiet periods is marked by the shaded bands, and the L-H transition with a long bar. Part (b) shows these same quantities over a longer 17.5 msec period for the same shot. These turbulence quantities were evaluated at ρ=0.4 cm (just outside the separatrix), and averaged over a time interval of ~40 μsec around each time point. Positive V_{pol} corresponds to the electron diamagnetic direction.

11. Time-delayed cross-correlation functions between F_{sol} and other turbulence quantities during a 3.5 msec period just before the L-H transition in #135042 (0.239505-0.243005 sec): (a) F_{sol} vs. V_{pol}, (b) F_{sol} vs. τ, (c) F_{sol} vs. L_{pol}, and (d) F_{sol} vs. S. For this figure the cross-correlations are shown for five adjacent radial regions within the box in Fig. 2, including the case for ρ = +0.4 cm used for Fig. 10 (green). The cross-correlations of F_{sol} and V_{pol} all show a peak near zero delay, but the time of this peak correlation changes systematically with radius. Cross-correlations of F_{sol} and S are strongest near the separatrix.

12. The time evolution of several of the quantities of Fig. 11 for the period up to ~30 msec before the L-H transition for the same three shots as in Fig. 9. In part (a) is the magnitude of the first negative peak of the autocorrelation function of F_{sol}, which is a rough measure of the size of the oscillating feature at ~3 kHz, and below that is the corresponding frequency of this feature. In part (b) is the magnitude of the peak of the cross-correlation functions between F_{sol} and V_{pol} near zero delay time, and below that is the delay time to this peak. In part (c) is the magnitude of the peak of the cross-correlation functions between F_{sol} and S (near zero delay), and below that the delay time to this peak.

13. Typical scatter plots of the correlation between F_{sol} and V_{pol} (left) and F_{sol} and S (right) for the same ρ=0.4 cm case used for the cross-correlation analysis of Fig. 11. Here both plots show all 1000 time points within a 3.5 msec period ending ~2 msec before the transition, with a small correction to align the time of the peak of their cross-correlations of Fig. 11. There appears to be a significant statistical correlation between quiet periods with low values of F_{sol} and a positive V_{pol}, as can also be seen in Fig. 10(a). The line in (a) is a linear fit to this data. There is a rather wide scatter of F_{sol} vs. S (right), independent of the radial averaging width $\delta\rho$ used for dV_p/dr (i.e. red vs. blue).

14. Analysis of the size and frequency of the ~ 3 kHz quiet feature vs. time for a larger database of shots, including the data previously shown in Fig. 12(a). The L-mode shots are put at -150 msec, and the H-mode shot is put at +50 msec, to bring them into the same plot. There is evidently no clear change in the size or frequency of the ~ 3 kHz feature just preceding the L-H transition, consistent with the trend seen in Figs. 10 and 12. The ~ 3 kHz feature also appears in L-mode and H-mode shots, so does not appear to be a feature specific to the L-H transition.

15. Time dependences of the edge quietness parameter F_{sol} and the normalized shear S for a period of ~15 msec before the L-H transition (red lines) for two additional shots besides #135042 (already shown in Fig. 10(b)). Although there is a strong modulation of S with F_{sol} at ~ 3 kHz for at least 15 msec before the transition, there are no clear variations in the average value of F_{sol} or S on this timescale, consistent with Figs. 10 and 12. A radial averaging of $\delta\rho$~1.5 cm was used for the velocity gradient in this analysis.

16. The normalized shear S for the time period up to $\leq$1.5 msec before the transition for three radial location for #135042 (left), and for the superposition of all 9 shots at the highest frame rate at the same radii (right). There is again no clear variation in S before the transition which could be considered as a trigger for the L-H transition. A radial averaging of $\delta\rho$~1.5 cm was used for the velocity gradient in this analysis.

(a)

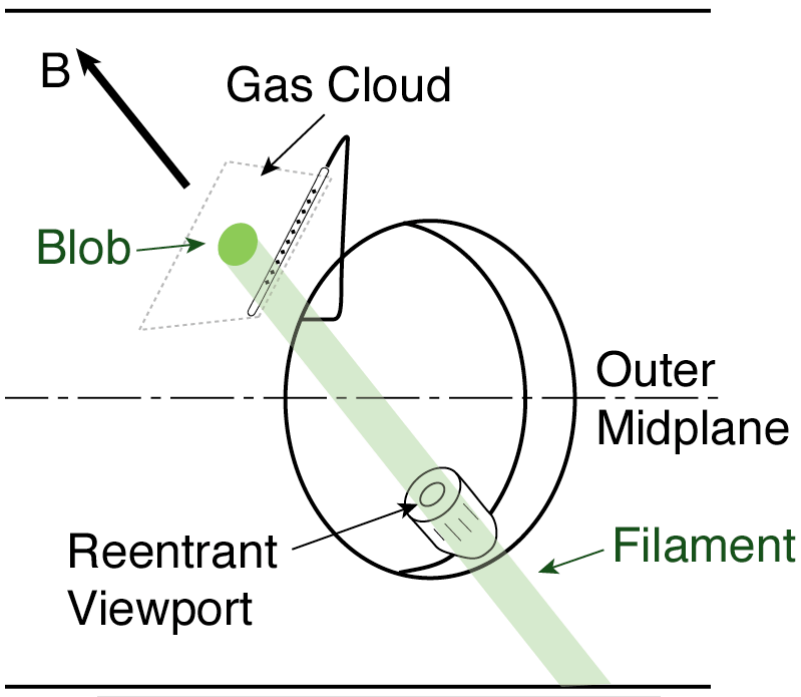
B
Gas Cloud
Blob
Outer
Midplane
Reentrant
Viewport
Filament

(b)

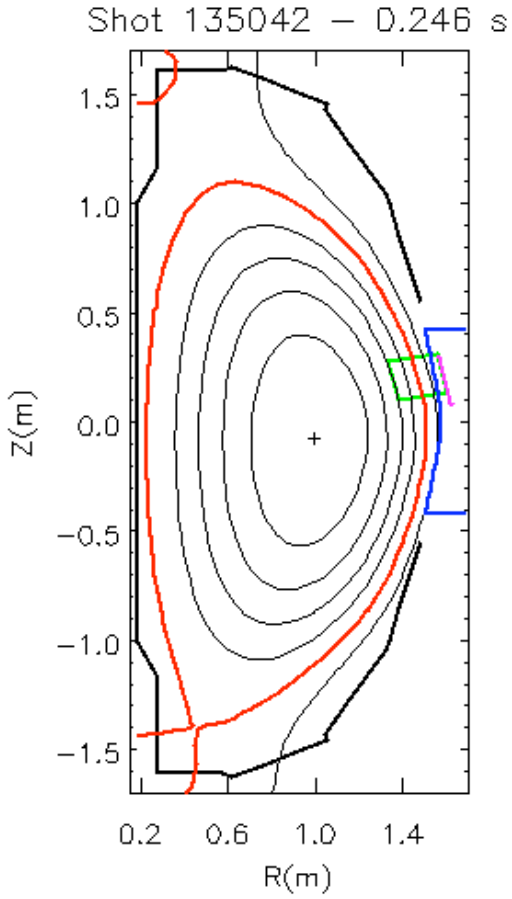
Shot 135042 – 0.246 s
1.5
1.0
0.5
0.0
−0.5
−1.0
−1.5
Z(m)
0.2
0.6
1.0
1.4
R(m)

Fig. 1

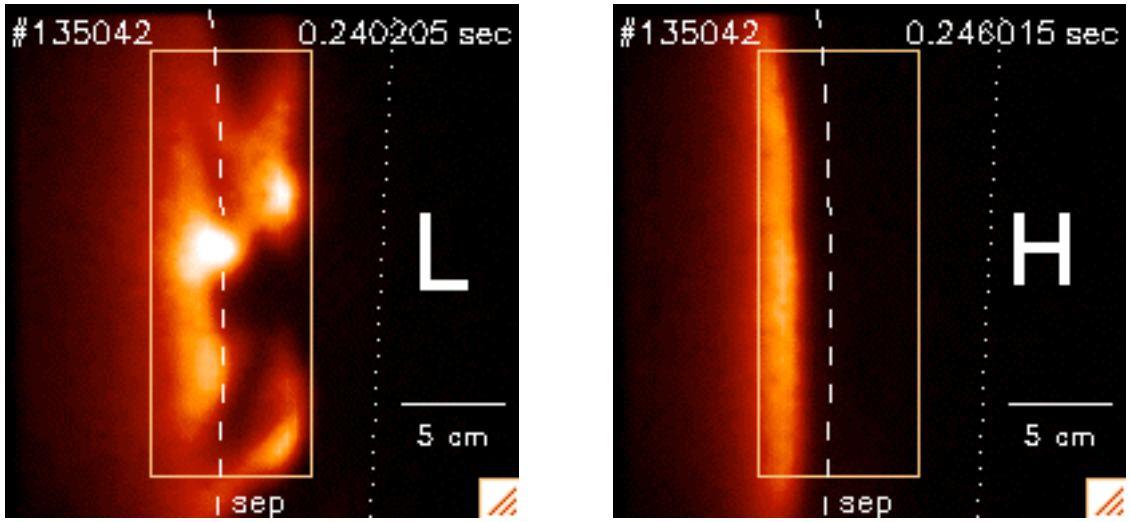

Fig. 2

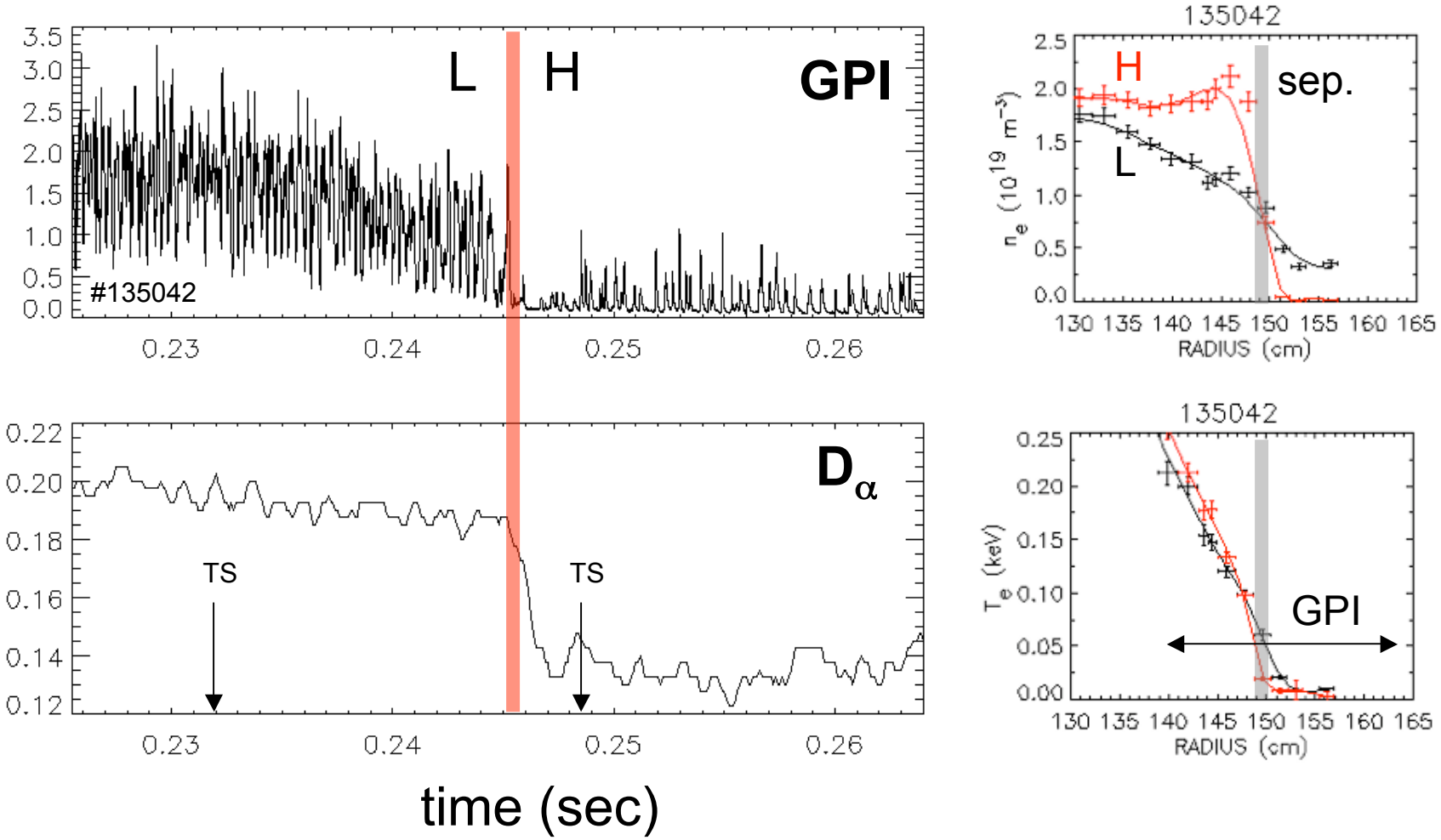
L
H
GPI
#135042
3.5
3.0
2.5
2.0
1.5
1.0
0.5
0.0
0.23
0.24
0.25
0.26
D_α
TS
TS
0.22
0.20
0.18
0.16
0.14
0.12
time (sec)
135042
H
L
sep.
n_e (10^{19} m^{-3})
RADIUS (cm)
135042
T_e (keV)
GPI
RADIUS (cm)

Fig. 3

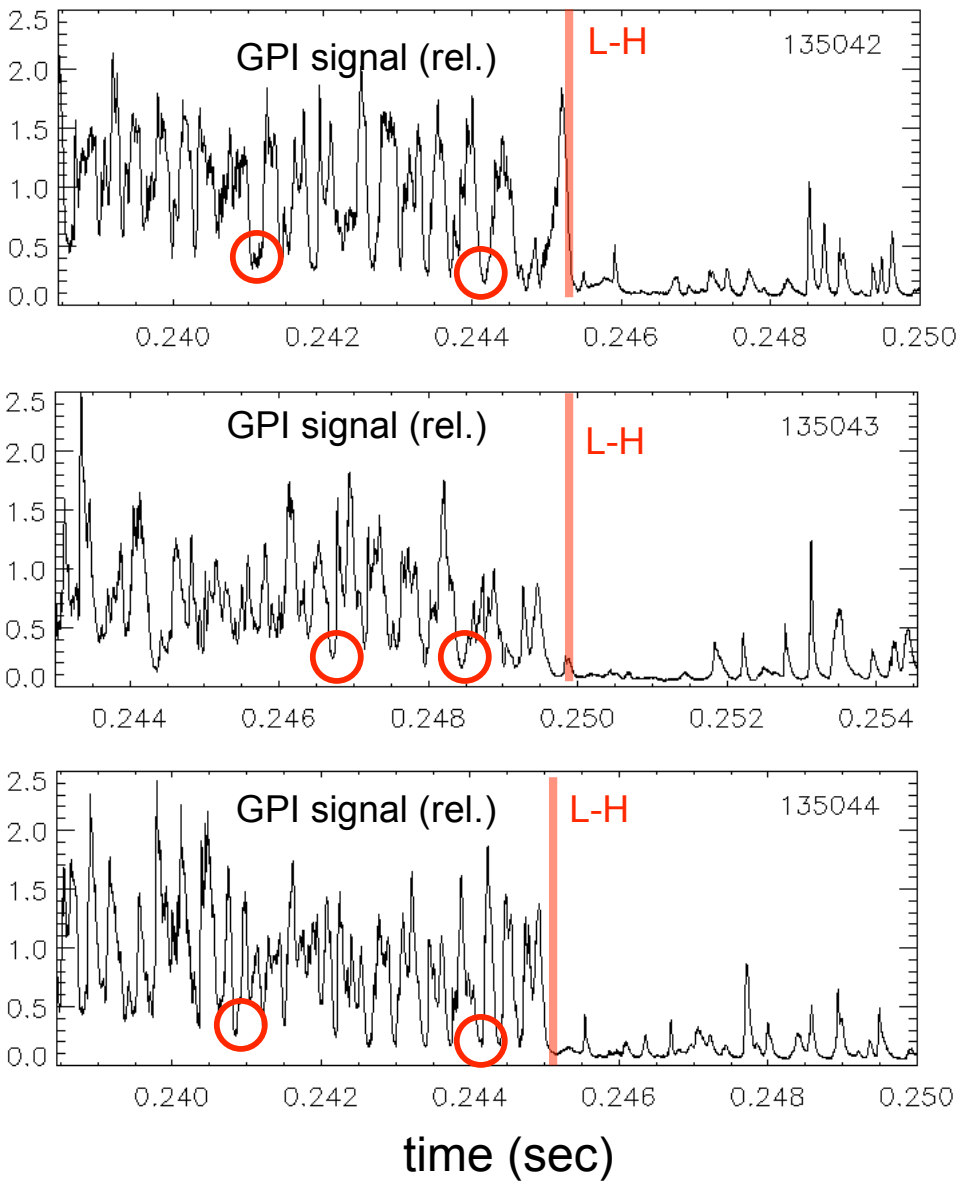
GPI signal (rel.)
L-H
135042
GPI signal (rel.)
L-H
135043
GPI signal (rel.)
L-H
135044
2.5
2.0
1.5
1.0
0.5
0.0
0.240
0.242
0.244
0.246
0.248
0.250
0.252
0.254
time (sec)

Fig. 4

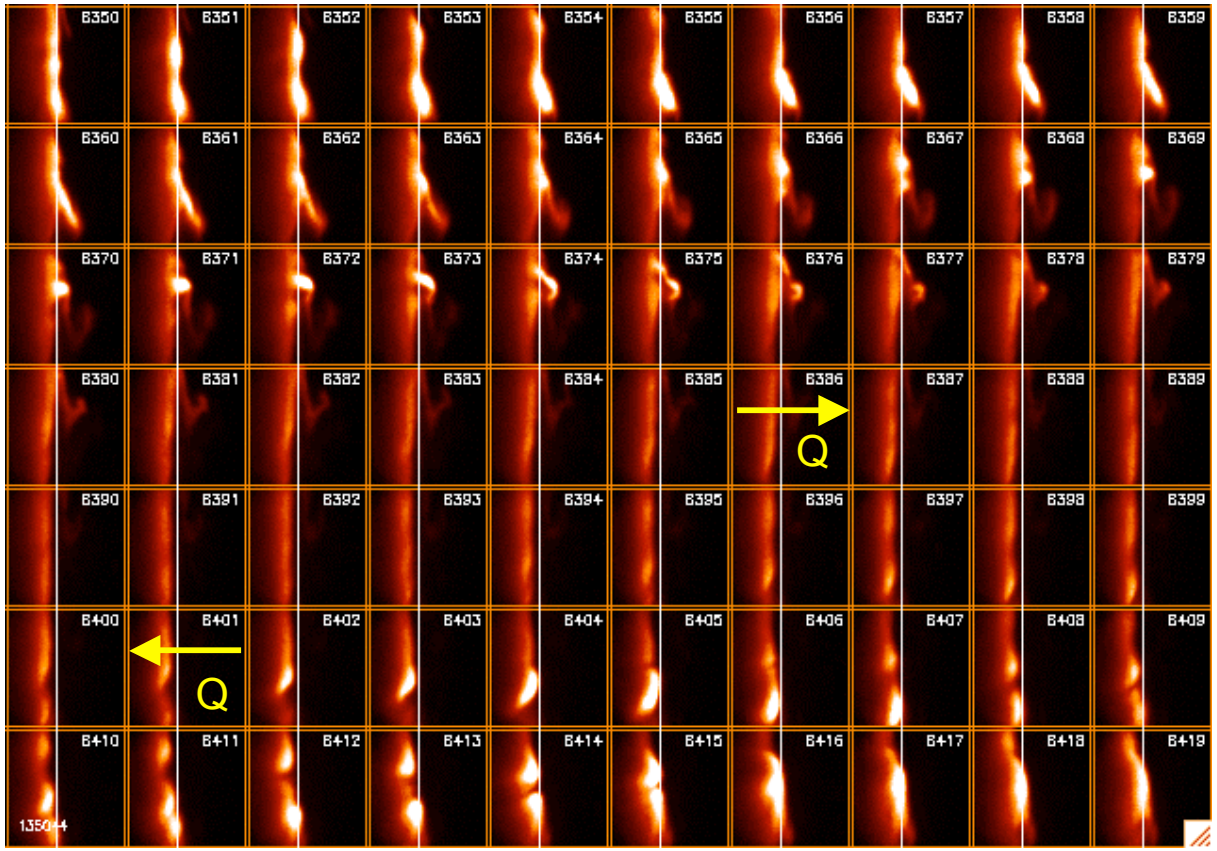

Fig. 5

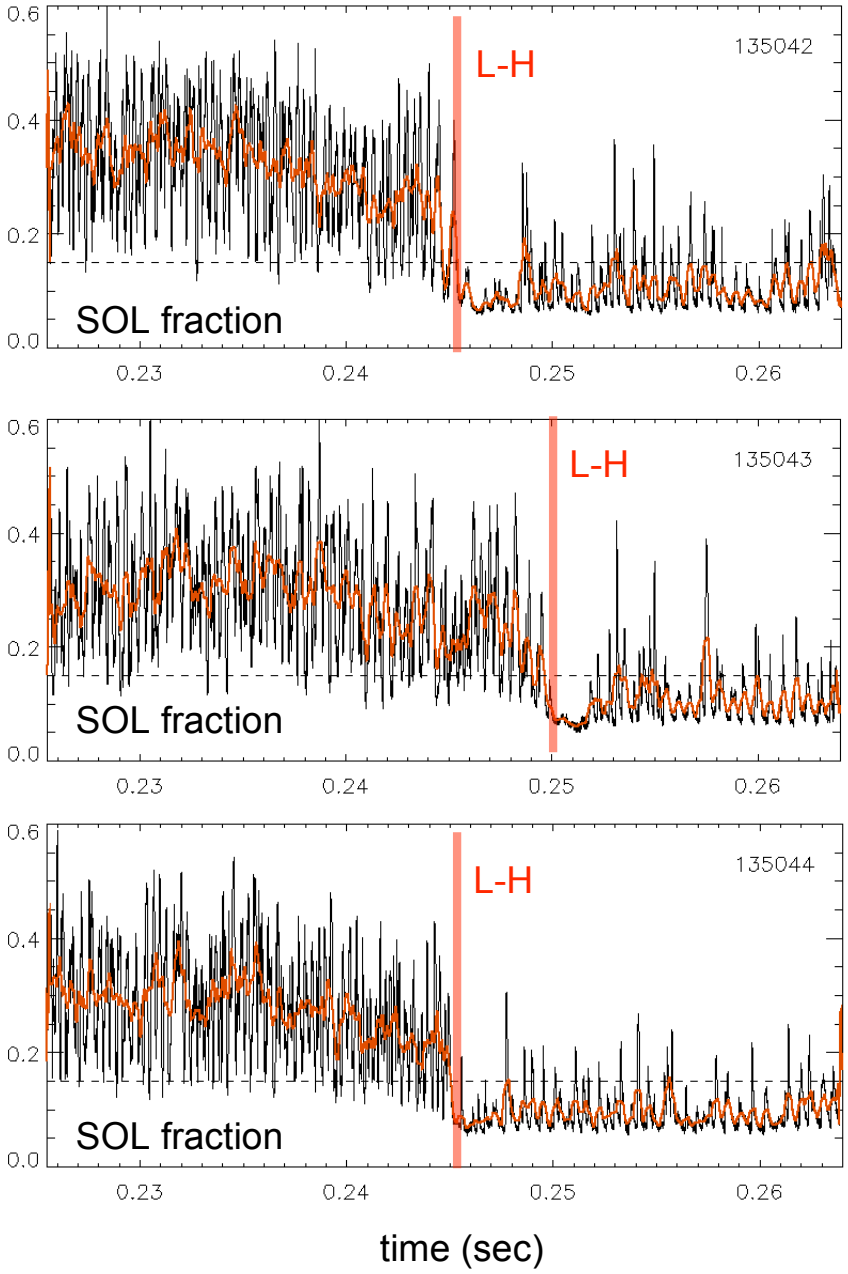
0.6
0.4
0.2
0.0
L-H
135042
SOL fraction
0.23
0.24
0.25
0.26
0.6
0.4
0.2
0.0
L-H
135043
SOL fraction
0.23
0.24
0.25
0.26
0.6
0.4
0.2
0.0
L-H
135044
SOL fraction
0.23
0.24
0.25
0.26
time (sec)

Fig. 6

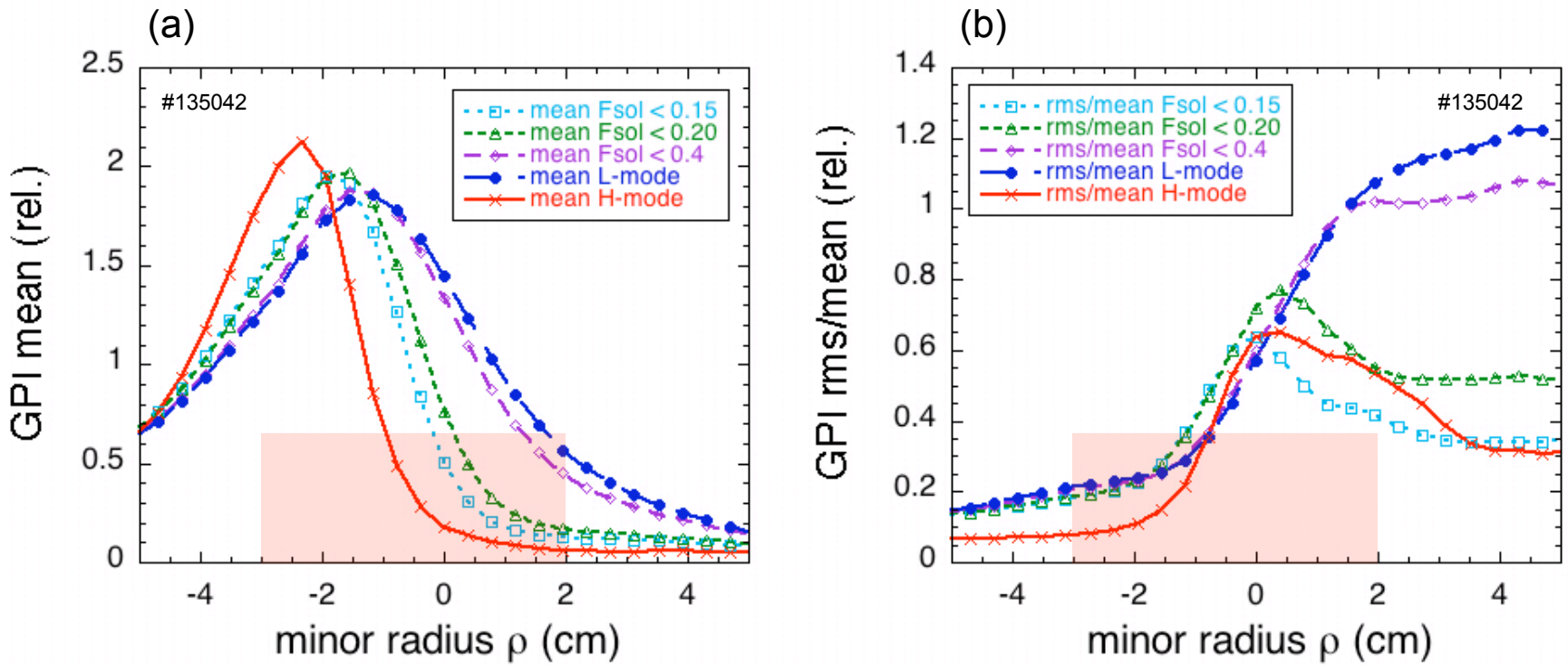
(a)
#135042
mean Fsol < 0.15
mean Fsol < 0.20
mean Fsol < 0.4
mean L-mode
mean H-mode
GPI mean (rel.)
minor radius ρ (cm)
(b)
#135042
rms/mean Fsol < 0.15
rms/mean Fsol < 0.20
rms/mean Fsol < 0.4
rms/mean L-mode
rms/mean H-mode
GPI rms/mean (rel.)
minor radius ρ (cm)

Fig. 7

(a) radial profile vs. time

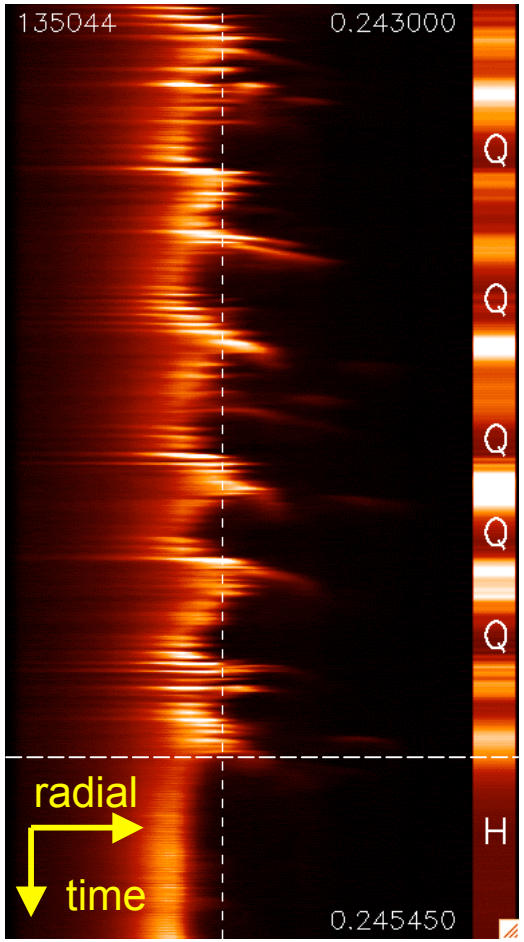

(b) poloidal @ ρ = 0 cm

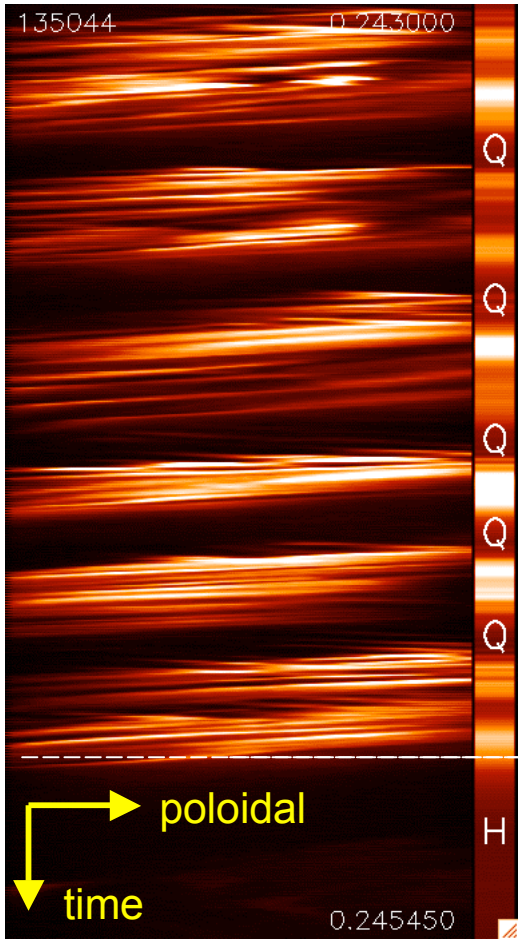

(c) poloidal @ ρ = -3 cm

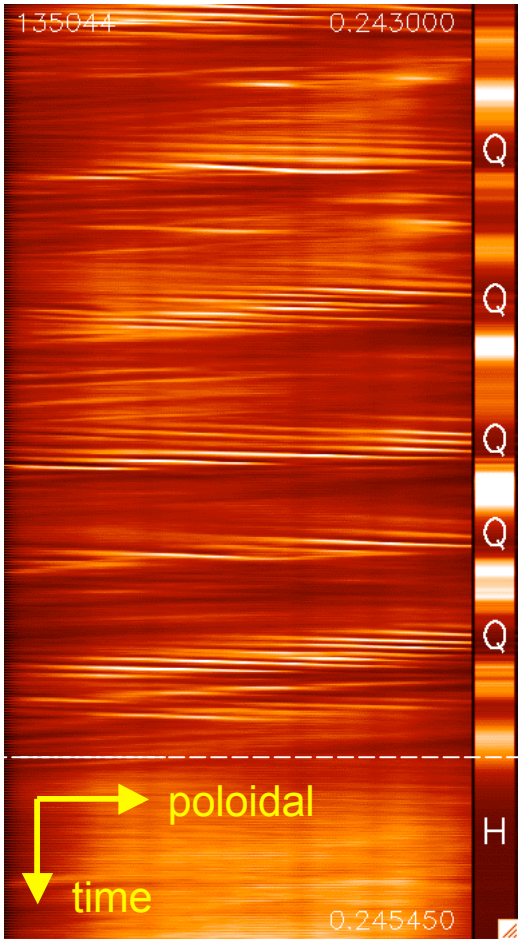

Fig. 8

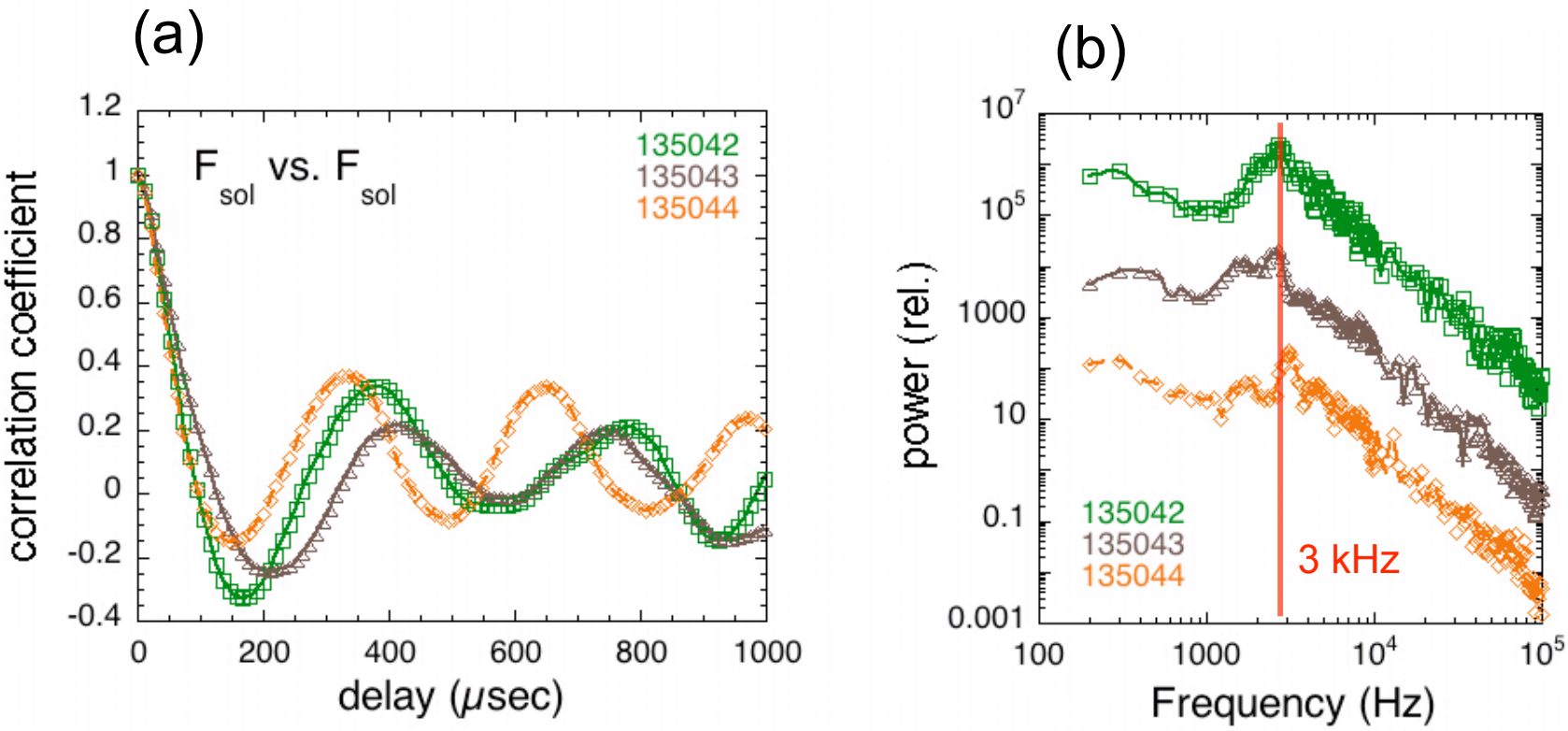
(a)
correlation coefficient
F sol vs. F sol
135042
135043
135044
1.2
1
0.8
0.6
0.4
0.2
0
-0.2
-0.4
0
200
400
600
800
1000
delay (μsec)
(b)
power (rel.)
10^7
10^5
1000
10
0.1
0.001
135042
135043
135044
3 kHz
100
1000
10^4
10^5
Frequency (Hz)

Fig. 9

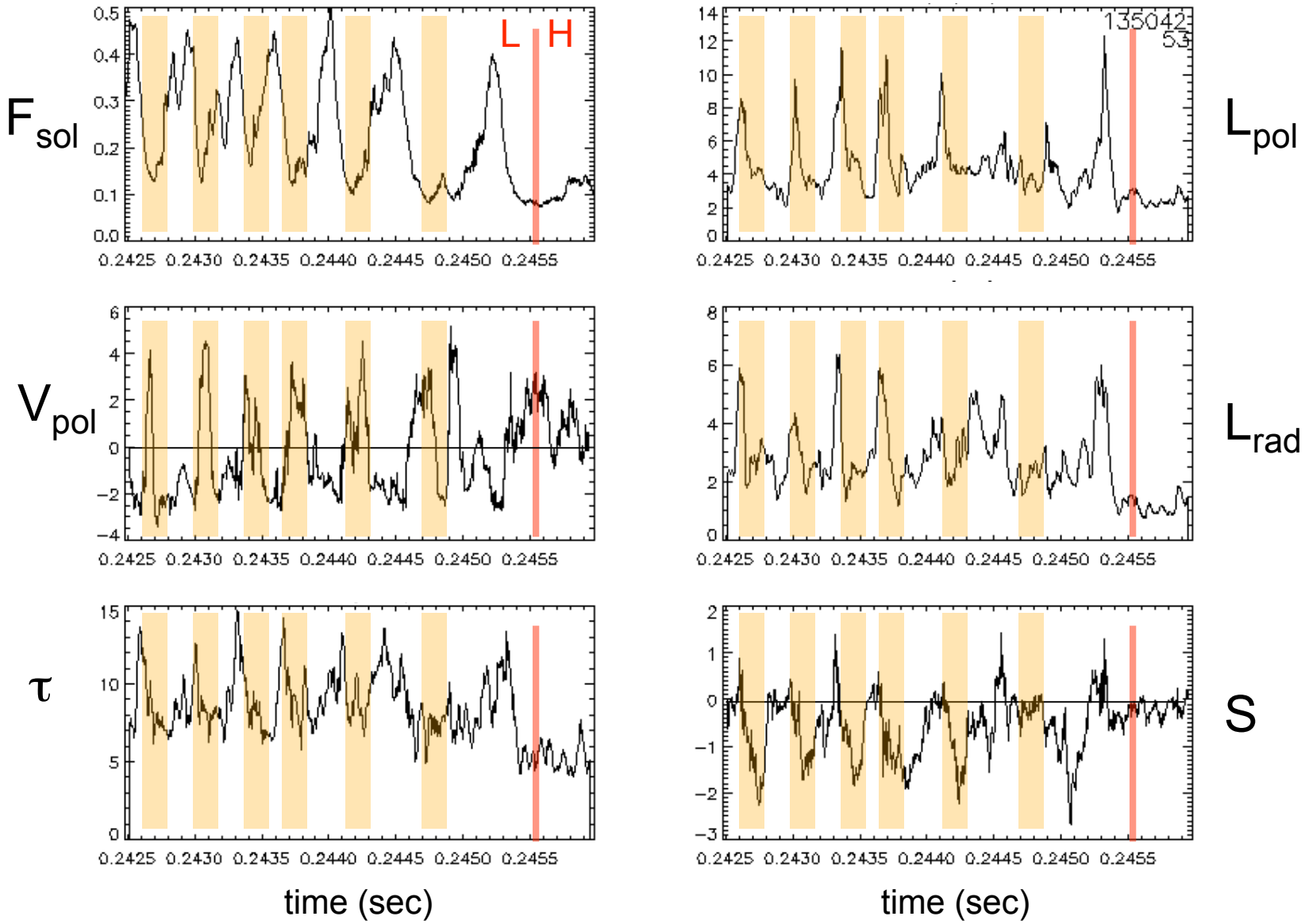
F_{sol}
L
H
L_{pol}
135042
53
V_{pol}
L_{rad}
τ
S
0.2425 0.2430 0.2435 0.2440 0.2445 0.2450 0.2455
time (sec)
time (sec)

Fig. 10(a)

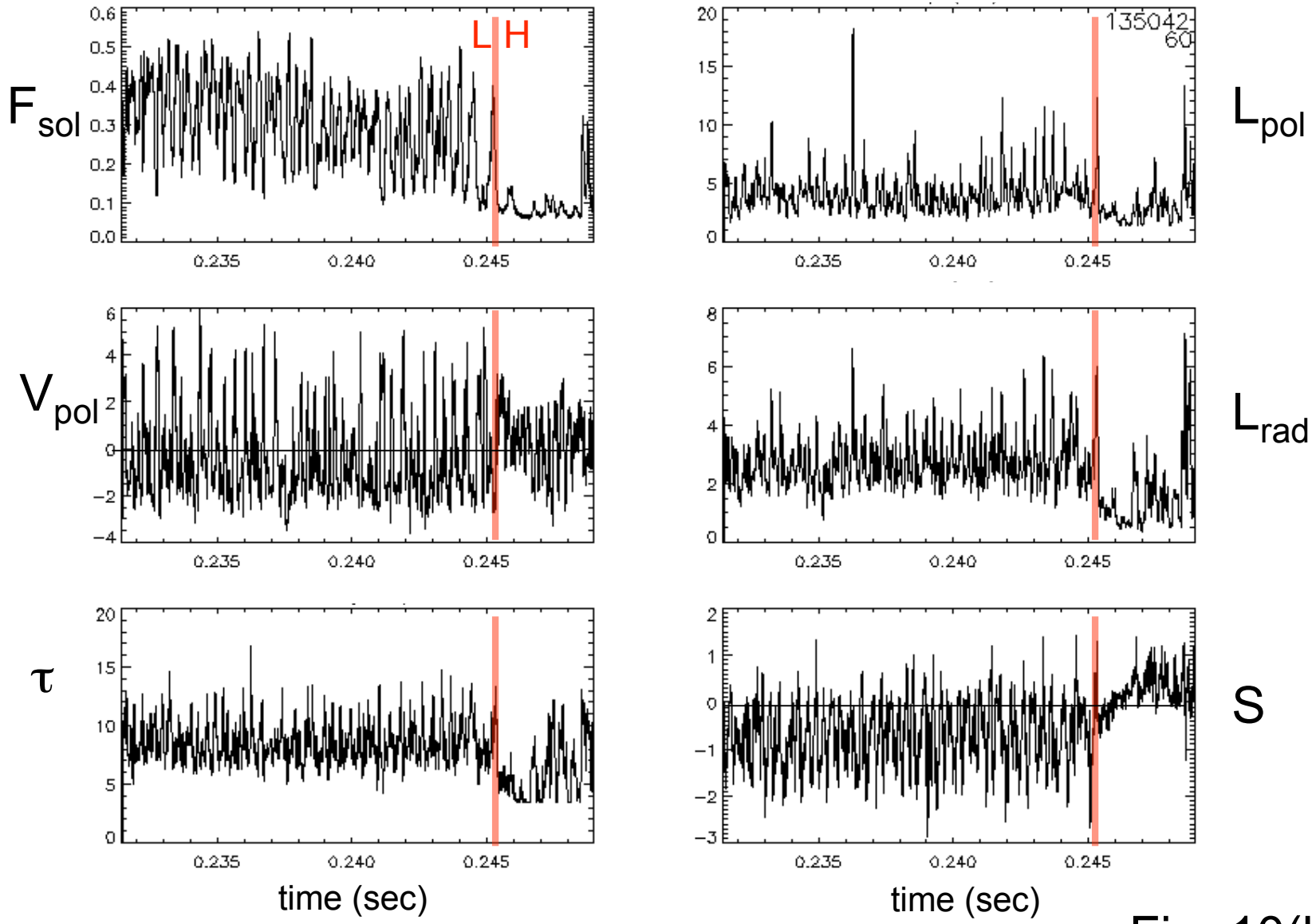
F_{sol}
L
H
L_{pol}
135042
60
V_{pol}
L_{rad}
τ
S
0.235
0.240
0.245
time (sec)
time (sec)

Fig. 10(b)

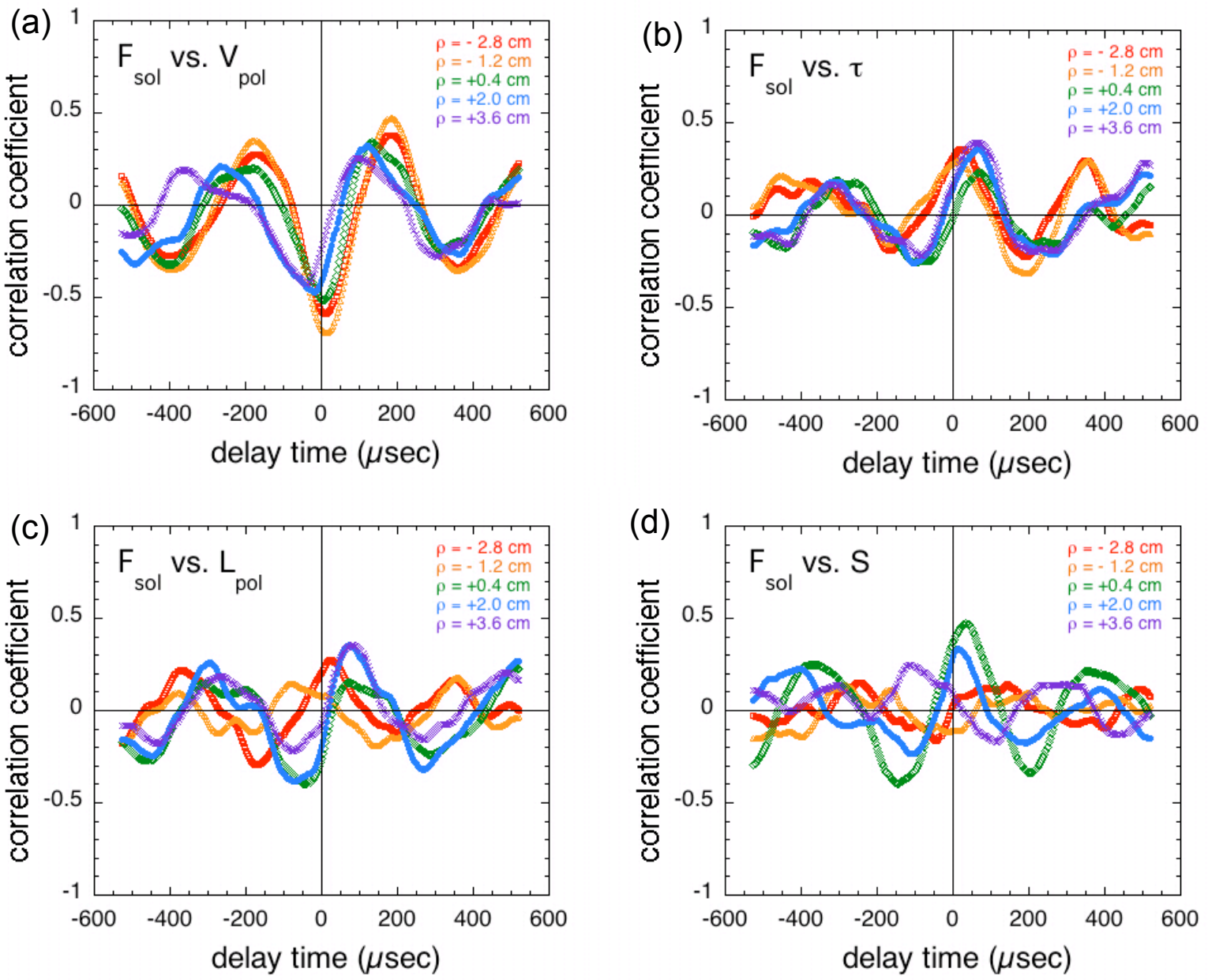
(a)
F sol vs. V pol
ρ = - 2.8 cm
ρ = - 1.2 cm
ρ = +0.4 cm
ρ = +2.0 cm
ρ = +3.6 cm
correlation coefficient
delay time (μsec)
(b)
F sol vs. τ
(c)
F sol vs. L pol
(d)
F sol vs. S

Fig. 11

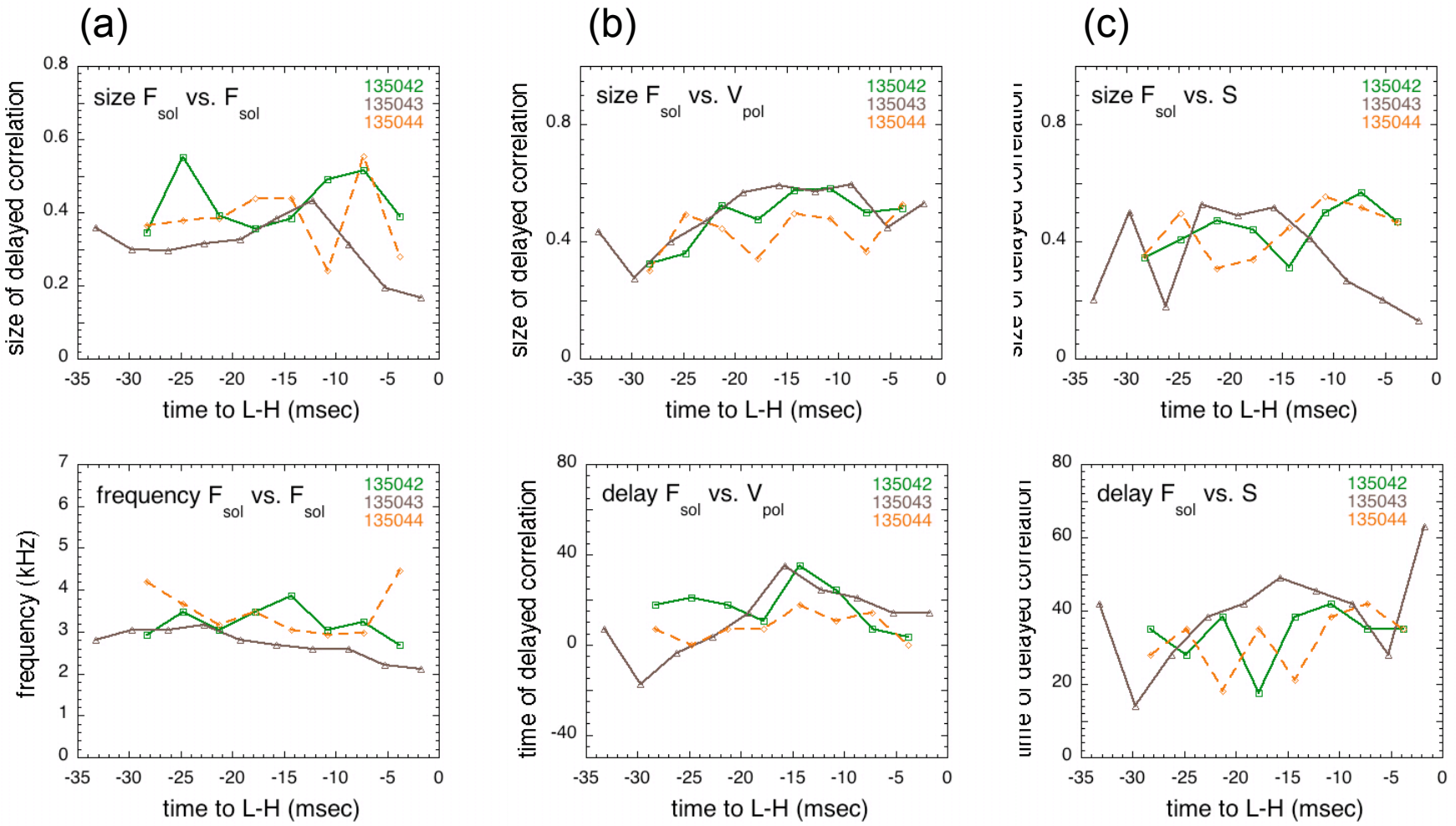
(a)
(b)
(c)
size F sol vs. F sol
size F sol vs. V pol
size F sol vs. S
frequency F sol vs. F sol
delay F sol vs. V pol
delay F sol vs. S
135042
135043
135044
size of delayed correlation
frequency (kHz)
time of delayed correlation
time to L-H (msec)

Fig. 12

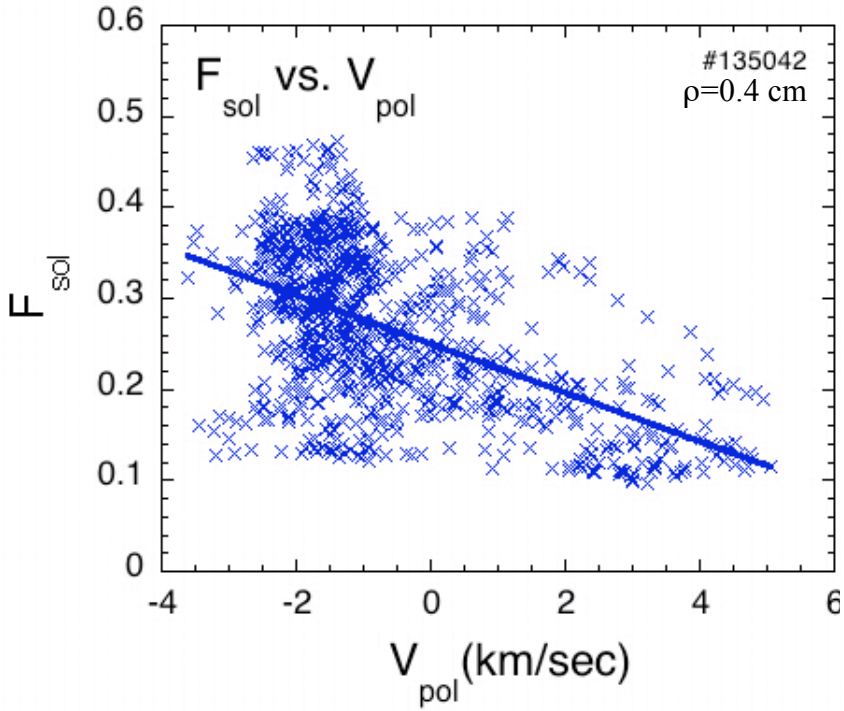
F sol vs. V pol
#135042
ρ=0.4 cm
F sol
V pol (km/sec)
0.6
0.5
0.4
0.3
0.2
0.1
0
-4
-2
0
2
4
6

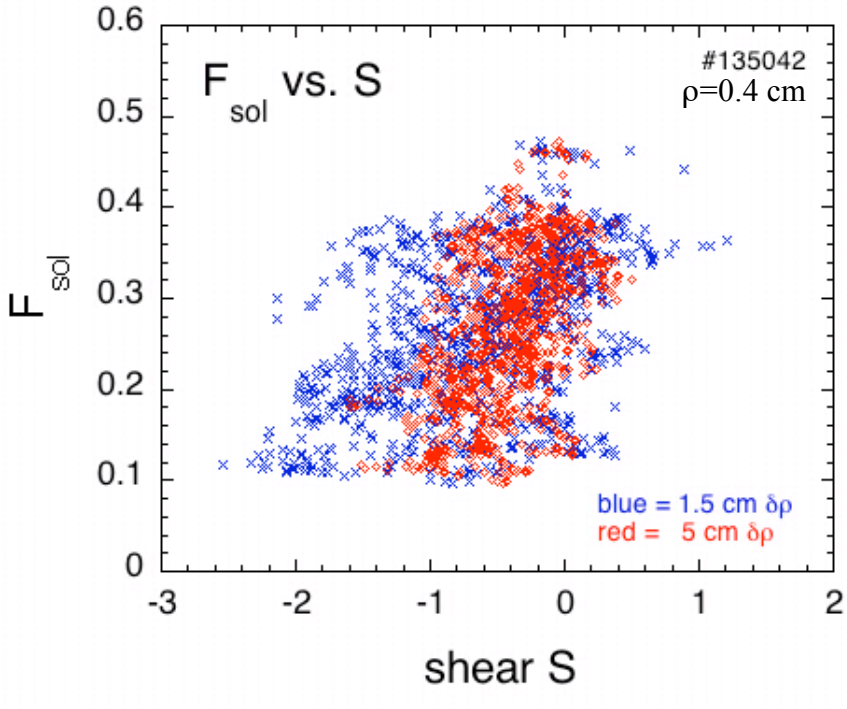
F sol vs. S
#135042
ρ=0.4 cm
blue = 1.5 cm δρ
red = 5 cm δρ
F sol
shear S
0.6
0.5
0.4
0.3
0.2
0.1
0
-3
-2
-1
0
1
2

Fig. 13

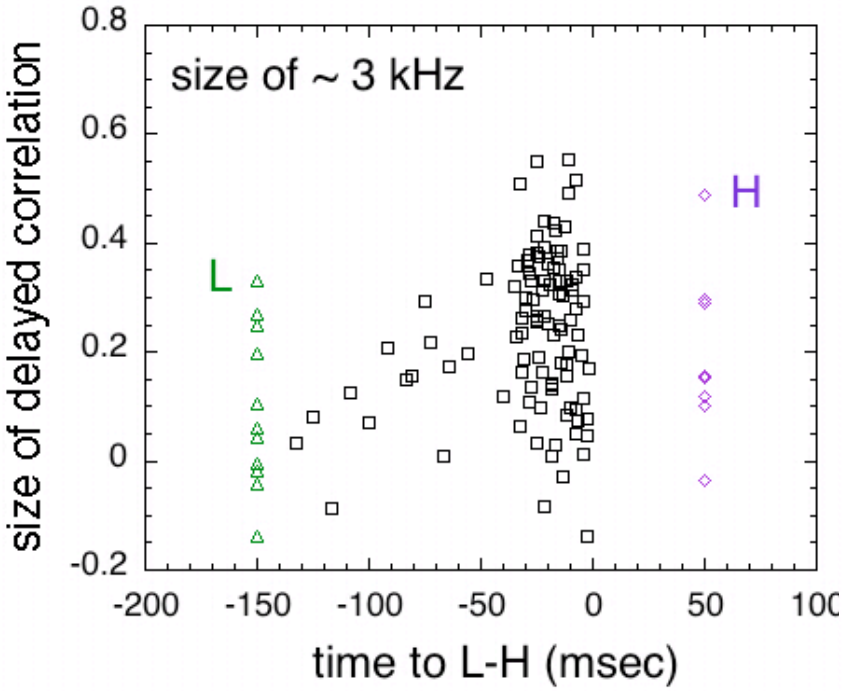
size of ~ 3 kHz
size of delayed correlation
0.8
0.6
0.4
0.2
0
-0.2
L
H
-200
-150
-100
-50
0
50
100
time to L-H (msec)

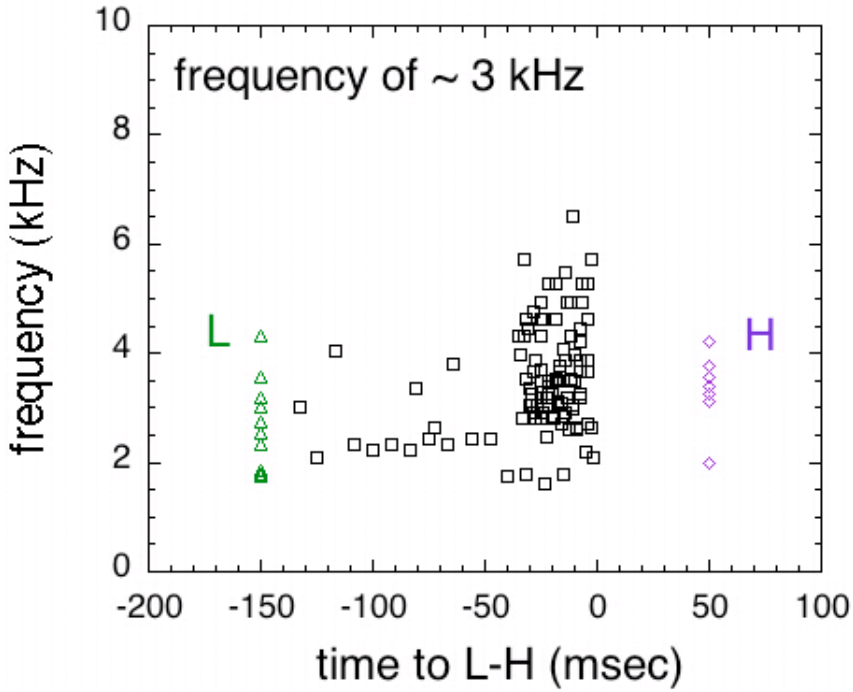
frequency of ~ 3 kHz
frequency (kHz)
10
8
6
4
2
0
L
H
-200
-150
-100
-50
0
50
100
time to L-H (msec)

Fig. 14

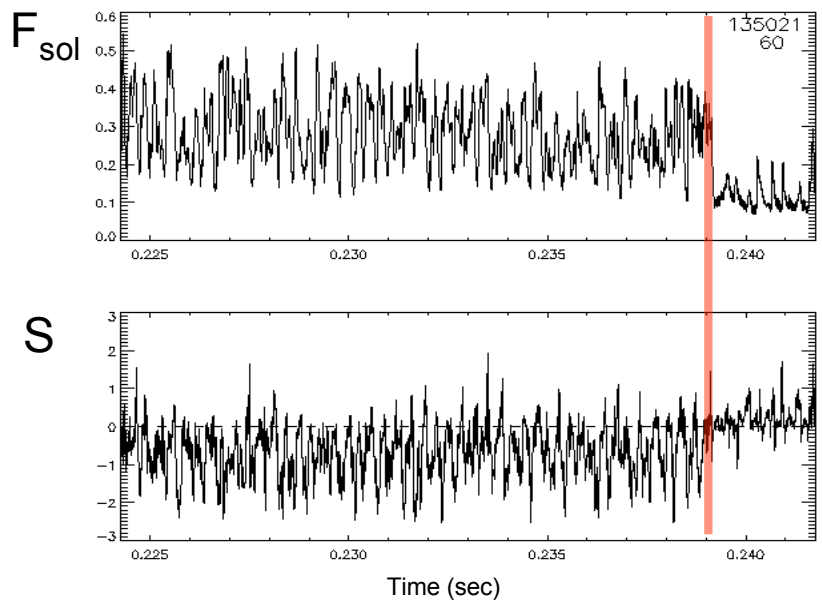

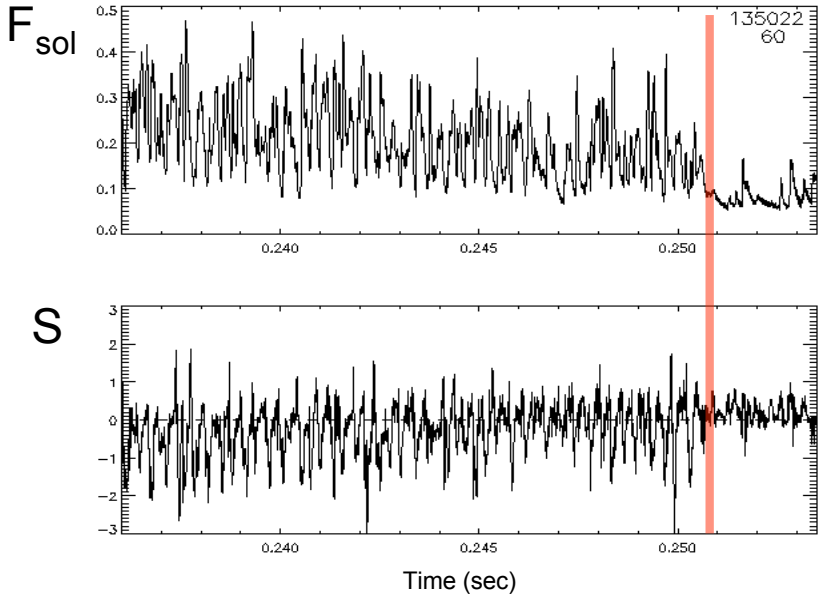

Fig. 15

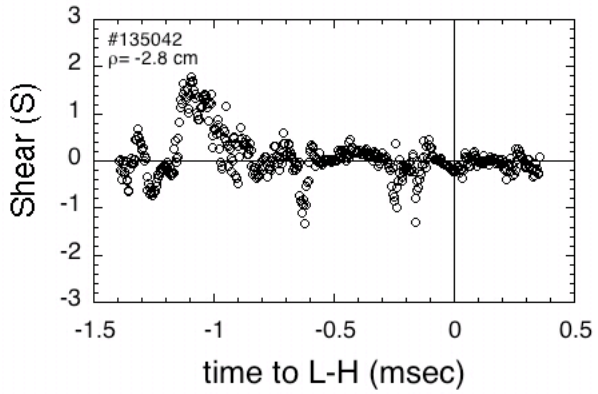
#135042
ρ= -2.8 cm
Shear (S)
time to L-H (msec)

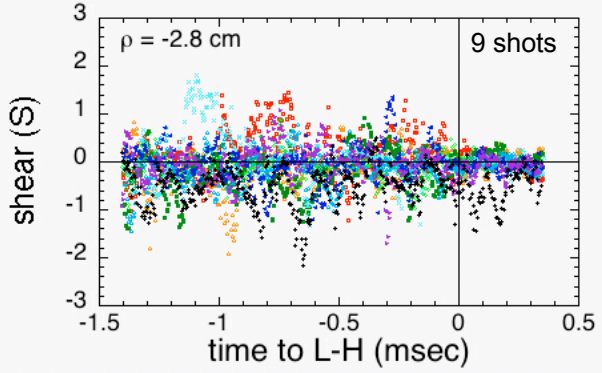
ρ = -2.8 cm
9 shots
shear (S)
time to L-H (msec)

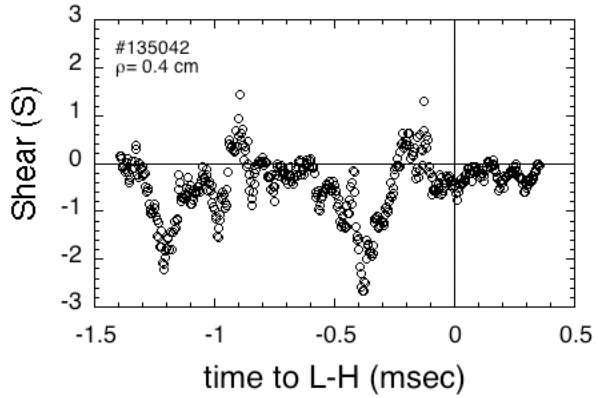
#135042
ρ= 0.4 cm
Shear (S)
time to L-H (msec)

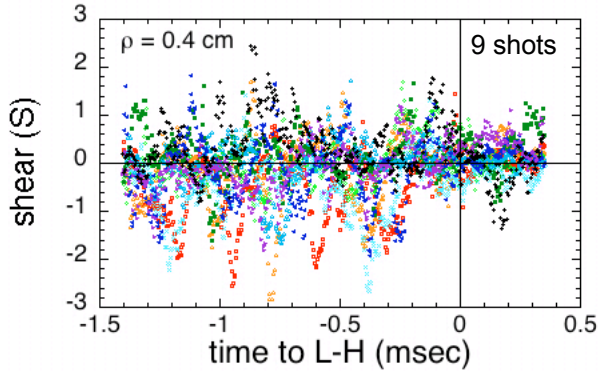
ρ = 0.4 cm
9 shots
shear (S)
time to L-H (msec)

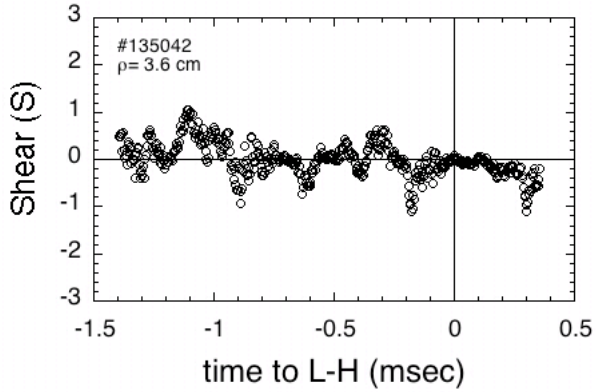
#135042
ρ= 3.6 cm
Shear (S)
time to L-H (msec)

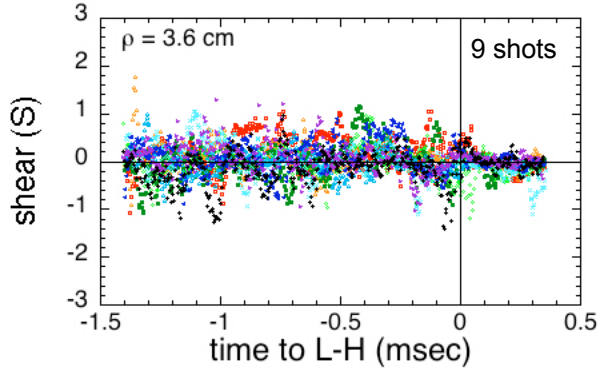
ρ = 3.6 cm
9 shots
shear (S)
time to L-H (msec)

Fig. 16

The Princeton Plasma Physics Laboratory is operated
by Princeton University under contract
with the U.S. Department of Energy.

Information Services
Princeton Plasma Physics Laboratory
P.O. Box 451
Princeton, NJ 08543

Phone: 609-243-2245
Fax: 609-243-2751
e-mail: pppl_info@pppl.gov
Internet Address: http://www.pppl.gov